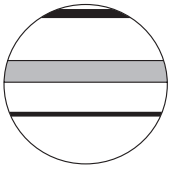

Research Paper

The Holocene
1–18

DOI: 10.1177/09596836231151828
journals.sagepub.com/home/hol
SAGE

Volcanic, tectonic and climate controls on lacustrine sedimentary supplies over the last millenia in NE Chilean Patagonia (Lake Esponja, Aysen, 45°S)

Nathalie Fagel,[1] Pablo Pedreros,[2] Denisse Alvarez,[2,3] Isabel Israde Alcantara,[4] Ignacio Vega Alay,[2] Olivier Namur,[5] Alberto Araneda,[2] Sabine Schmidt,[6] Gilles Lepoint[7] and Roberto Urrutia[2]

Abstract

The environmental variability of Northern Chilean Patagonia during the last millennia is evaluated using a multi-proxy analysis of sediment cores from Lake Esponja (45°S 72°W) to decipher if the sediment deposition is controlled by volcanic eruptions, landslides induced by earthquake or heavy rainfall. The lake is located in a glacio-tectonic valley in Patagonia. The organic-rich clayey silt sediment with low biogenic silica content was analysed for grain size, magnetic susceptibility, organic matter, biogenic silica content and diatom assemblages, mineralogy (X-ray diffraction), organic (IRMS C and N analyses) and inorganic (XRF core-scanner) geochemistry and glass shard major composition (Microprobe, SEM). The combination of ^{210}Pb, ^{137}Cs, ^{14}C and tephrochronology indicates an averaged accumulation rate of 0.4 mm/year, leading to a record of ~3.5 kyr within 154 cm. The sedimentary geochemistry records changes in volcanic supplies, diatom productivity and detrital inputs. The sediments were interrupted by millimetric to centimetric layers corresponding to tephra deposition related to explosive eruptions of nearby volcanoes Macá, Melimoyu and Hudson. Concerning the diatoms, the dominant planktonic species (80–150 cm) are replaced by benthic species in a transition interval (55–80 cm) and then by Surirella spp. in the upper core. This last genus indicates a closure of the basin ~2 ka ago, probably related to an uplift linked to a rejuvenation of the Mañihuales fault. This local change could reflect regional tectonic instability. Indeed, a partial earthquake rupture occurred around ~AD100 along the southern part of the Valdivia segment, recorded as a mass transport deposit in Aysén fjord sedimentation. The fine detrital input varies over time with more variable Si/Al values in the lower part of the LEs14 core than in the upper 80 cm. The higher values may reflect wetter conditions, leading to an higher lake level and more turbid conditions in agreement with changes in diatom assemblages.

Keywords

Chile, diatom assemblages, Lacustrine sediment, Late-Holocene, sedimentary geochemistry, tephra

Received 10 March 2022; revised manuscript accepted 30 November 2022

Introduction

Lacustrine sediments have been widely used as a reliable archive for climatic reconstructions in particular over the Holocene (e.g. Bradley, 1999). However, the approach requires to unambiguously evidence any event deposit that interrupted the background sedimentation to elaborate a robust age model. Those events may record regional tectonic activities related to earthquakes (Chapron et al., 1999), volcanic eruptions (e.g. Fontijn et al., 2014; Naranjo and Stern, 2004), landslides or earthquake-induced landslides (e.g. Siegenthaler and Sturm, 1991). They may also register climatic changes like debris flow related to heavy rainfall (Moreiras, 2005; Sepúlveda et al., 2006), snowmelt or even anthropogenic activities (e.g. Guyard et al., 2007; Waldmann et al., 2011).

In Chile, in particular, the Southern Volcanic Zone (SVZ) of the Chilean Andes is characterised by numerous lakes that are affected by a complex interplay of tectonics and volcanism (Cembrano and Lara, 2009). Regional tectonic is mainly controlled by the oblique convergence between the Nazca and South American

[1]AGEs - Clays, Sedimentary environments and Geochemistry, Department of Geology, Université de Liège, Belgium
[2]Faculty of Environmental Sciences and EULA - Chile Environmental Sciences Centre, University of Concepcion, Chile
[3]Centro Bahía Lomas, Facultad de Ciencias, Universidad Santo Tomás, Chile
[4]Instituto de Investigaciones en Ciencias de la Tierra, Universidad Michoacacana de San Nicolás de Hidalgo. Morelia, Michoacán, Mexico
[5]KUL, Belgium
[6]UMR Environnements et Paléoenvironnements Océaniques et Continentaux, Université de Bordeaux, France
[7]Laboratory of Oceanology, Department of Biology, Université de Liège, Belgium

Corresponding author:
Nathalie Fagel, AGEs - Clays, Sedimentary Environments and Geochemistry, Department of Geology, Université de Liège, Allée du 6 août 14, B18, Quartier Agora, Liège 4000, Belgium.
Email: Nathalie.fagel@uliege.be

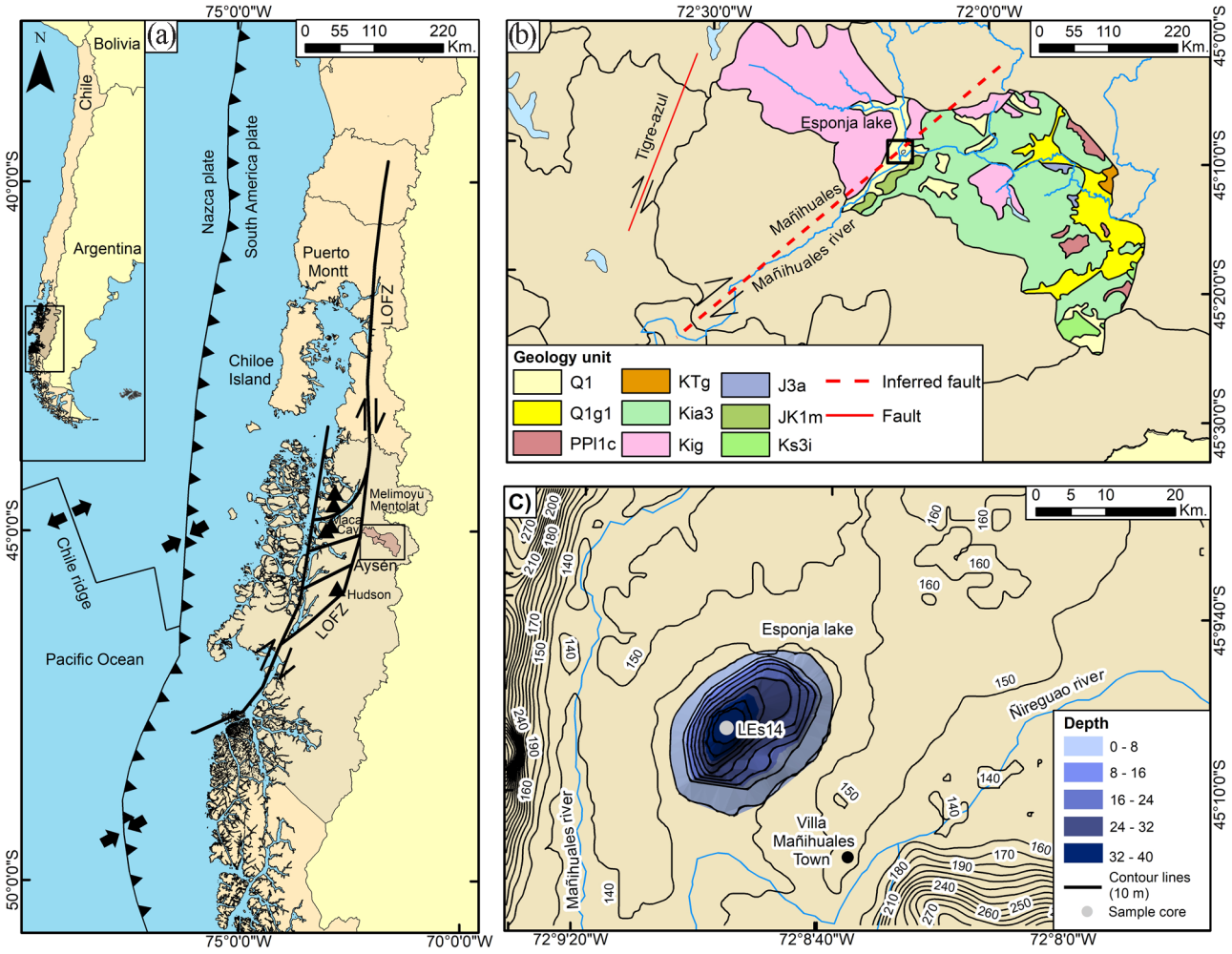

Figure 1. (a) Location of Lake Esponja within the Aysén region of Chile. The location of the Hudson, Macá, Cay, Melimoyu and Mentolat volcanoes is reported on the map by triangles. (b) Geology of the watershed of Lake Esponja and adjacent watersheds (data from SERNAGEOMIN, 2003, http://portalgeominbeta.sernageomin.cl/, consulted on July 2021). The lake watershed is made by three sub-watersheds of 308, 674, and 144 km^2 of superficial, respectively. The lake location is given by the black square. The main geological terranes are Late Jurassic/Cretaceous granites and granodiorites (Kig); dacitic to rhyolitic lavas and pyroclastic deposits of the Late Jurassic Ibanez Formation (J3a) with some marine sedimentary deposits (Jk1m); andesitic to rhyolitic lavas and tuffs of the Early Cretaceous Divisadero Formation (Kia3); Quaternary alluvial deposits (Q1); Plio-Pleistocene alluvial deposits (PPl1c); Morainic, fluvio-glacial and glacio-lacustrine deposits Fluvio-glacial deposits (Q1g1). (c). Topography and bathymetry data of the Lake Esponja surroundings. The dotted red line gives the inferred position of the local fault named 'Rio Mañihuales fault' reported in Thomson (2002) and SERNAGEOMIN digital map (SERNAGEOMIN, 2003).

plates (Figure 1a) and the associated orogeny of the Andes (Sepúlveda et al., 2006). The resulting volcanic activity comprises alignments of strato-volcanoes on ancient faults of the volcanic arc (Cembrano and Lara, 2009; Legrand et al., 2011) and monogenic cones located in the vicinity of the Liquiñe-Ofqui Fault Zone (LOFZ) (Cembrano et al., 2000). LOFZ is an active trench-linked structure associated to an intra-arc shear zone (Cembrano et al., 2000). Beside recent major seismic activity (e.g. the 1960 Great Chilean earthquake in Valdivia on May 1960 corresponding to the strongest magnitude (Mw 9.5) ever instrumentally-recorded – Kanamori (1977); the seismic swarm (Mw 6.2) occurring in Aysen Fjord in 2007 and associated rockslide-induced tsunami – for example Vanneste et al. (2018), paleoseismic activities have been more and more evidenced by mass-wasting deposits in fjords and lakes from SVZ (Chapron et al., 2006; Moernaut et al., 2007; Van Daele et al., 2013; Wils et al., 2018, 2020). Most of the earthquake-induced landslides occurred along the LOFZ in the Andes (Chapron et al., 2006).

The aim of this study is to identify the main controls on the lacustrine productivity and sediment deposition in an active tectonic area of North Chilean Patagonia over the last four millennia. Sedimentological, geochemical and biological proxies are combined to understand the sources and origin of the particles that settle down at the lake bottom. The temporal evolution of abiotic proxies is further compared with the evolution of the biological assemblages to reconstruct the environmental conditions prevailing in the watershed. In an active tectonic area such as Patagonia, the identification of both regional and local volcanic and tectonic-related perturbations in the LEs record is a prerequisite for further paleoclimate reconstruction.

Study area

Lake Esponja (45°09′S, 72°08′W) is a small closed lacustrine system (0.25 km^2) located in Villa Mañihuales town (Figure 1). The lake bathymetry marked a maximum depth of 42 m. This lake is a perched lake set in a wide NNE-SSW valley extending ~60 km SW to Puerto Aysén (Figure 1a) bypassed by the west by the river Mañihuales (Figure 1b) and by the south by the river Ñireguao (Figure 1c). Mañihuales valley is of tectonic-glacial origin. The LOFZ (Figure 1a) is the main structural feature of the area (Charrier et al., 2007) corresponding to an active dextral strike-slip lineament system (Cembrano et al., 1996; Hervé, 1994). The local transpressional dextral fault (i.e. called the Rio Mañihuales fault, Thomson, 2002 – see location on Figure 1b), oriented NNE-SSW, is related to the overall geometry of the LOFZ fault (Figure 1a).

Landslides, debris flows and local rock falls were observed in Villa Mañihuales area (see location on Figure 1c). Mass wasting was locally triggered by intense precipitations along steep slopes (SERNAGEOMIN, 2012) and they may be regionally recorded in the Aysén fjord by density-flow deposits with reworked tephra (Van Daele et al., 2013).

Besides, the watershed of the lake is in the active volcanic area of the Southern Volcanic Zone (SVZ – Stern, 2004). It is located east of five volcanoes (see location on Figure 1a), among them the Macá and the Hudson are the most active. The recent, historical and prehistorical eruption activity was intensively studied in particular in lake records (e.g. Fontaine et al., 2021; Fontijn et al., 2014; Haberle and Lumley, 1998; Naranjo and Stern, 2004; Watt et al., 2013). The main widespread tephra layers are related to the explosive eruptions of the Hudson, Macá, Mentolat and Melimoyu volcanoes (Naranjo and Stern, 1998, 2004; Watt et al., 2013).

Regional geology is made by two main units (Pankhurst et al., 1999; SERNAGEOMIN, 2003). The North Patagonian batholith, on the western side, is mainly composed by Late Jurassic/Cretaceous granites and granodiorites (Figure 1b). On the eastern side continental Mesozoic volcanic sequences are intercalated with some sedimentary marine deposits. The Late Jurassic Ibañez Formation is made by dacitic to rhyolitic lavas and pyroclastic deposits and the Early Cretaceous Divisadero Formation by andesitic to rhyolitic lavas and tuffs. Quaternary and Plio-Pleistocene alluvial deposits, morainic and fluvio-glacial deposits occur along rivers.

Patagonia is located within the mid-latitude 30–60°S belt, between the Intertropical Convergence Zone to the North and the Antarctic Convergence Zone to the South. Its climate variability over the Holocene is mainly controlled by the intensity and/or latitudinal position of the Southern Westerlies Winds (SWW) (e.g. Gilli et al., 2005; Markgraf, 1993). Some authors suggested millennial changes in the strength of the SWW since the last glaciation without major latitudinal migration (Villa-Martinez et al., 2012), other ones rather proposed a latitudinal migration of SSW over the Holocene (Bertrand et al., 2014; Markgraf et al., 2003; Perren et al., 2020). At present, SWW bring heavy precipitation over the western side of southern South America but generate arid conditions on the eastern side of the Andes (Garreaud et al., 2013).

The regional climate is humid and temperate with rainy winter and short dry mild to cold summer, corresponding to the class Cfb to Cfc of the classification of Köppen (Peel et al., 2007). The meteorological station of Villa Mañihuales (45°10′27.45″S, 11°72°8′52.58″E) reports an annual average of cumulated precipitation of 1484 ± 367 mm and temperature of 9.2 ± 0.6°C between 1986 and 2013 interval (Data from DGA). The warmest month (February) is characterised by an average temperature of 14.6 ± 1.7°C and low averaged precipitation (60 ± 42 mm). The wetter month (June) presents an average precipitation of 198 ± 103 mm and cold temperature (4.2 ± 1.3°C). The vegetation corresponds to an intermediate ecotone, comprised between the western humid zone and the eastern steppic zone, characterised by forest of Nothofagus pumilio (Lenga beech) (Hepp et al., 2018; Luebert and Pliscoff, 2006). During the 20th century the forest has been strongly reduced by human-induced fires and replaced by herbaceous species to produce grasslands in the valley (Bizama et al., 2011).

Material and methods

Sedimentological and biological analyses

Three cores LEs11A (109 cm), LEs13 (23.5 cm) and LEs14 (155 cm) were collected using an Uwitec® gravity corer during different fieldtrips in 2011, 2013 and 2014, respectively. LEs14, that is the main core investigated in this study, was retrieved in the deepest part of the lake (42 m) at 45°09′54.3″ latitude S and 72°08′55.9″ longitude W (Figure 1c) whereas the two other cores were retrieved at 40 m depth. The core LEs13 was cut at 5 mm for geochronological purpose. The cores LEs11A and LEs14 were cut longitudinally. One half-core section (i.e. archive section) was described, photographed and measured by magnetic susceptibility (MS) with a Bartington® magnetic susceptibility metre MS2E point sensor with a 5 mm sampling interval. The correlation between the cores LEs11A and LEs14 is reported at Supplemental Material Figure 1, available online. For LEs14, the half-core working sections were further subsampled into 25 cm long × 4 cm wide × 1.5 cm deep aluminium boxes. The remaining sediment material was subsampled at 2.5 cm for organic content measurements by Loss-On-Ignition (LOI) (Heiri et al., 2001).

The sediment grayscale levels and XRF elemental core scanning were measured using a Scopix X-ray image-processing system (58 kV, 10 mA) and an Avaatech XRF core scanner with a Fe-Mo tube at the EPOC laboratory (Université de Bordeaux, France). The measurements were performed on the aluminium boxes. The XRF core scanning was done for 15 elements (i.e. from Al to Ba) at 10, 30, and 50 KV and 15, 20, and 25 s exposure time, respectively. Elemental ratios of Zr/Rb, Ca/Ti, Br/Ti and Si/Al were tested to reconstruct the grain-size and/or the origin of the sedimentary supplies (Carrevedo et al., 2015; Kalugin et al., 2013; Kylander et al., 2011, 2012; Wang et al., 2011).

To complete the sedimentological description, grain-size data were determined at a sampling resolution of 2 cm for LEs14 ($n = 79$). Grain-size analysis was performed by a laser Malvern® Mastersizer 2000 diffraction particle analyser at the ARGENCO Department (Université de Liège). The bulk sediment samples were sieved at 2 mm, dispersed in deionised water and introduced into the Hydro 2000G dispersion unit. The sample amount was adjusted to reach an optimal laser beam obscuration of 15% ±5. The sampled was then homogenised with a 2000 rpm stirrer and disaggregated with 20% of ultrasonic waves. The analysis was triplicate to ensure the reproducibility of the data. The grain-size parameters (i.e. mean and percentile) were calculated according to Folk and Ward (1957).

The mineralogical phases were identified by X-ray diffraction (XRD) on LEs14 ($n = 27$) with an averaged sampling step of 10 cm. Some additional samples were selected on coarse layers in LEs 14 and from the main tephra layer of LEs11 to confirm the presence of glass phases. The 40°C-dried and crushed <150 microns sediment sample powder was measured by the backside method described by Moore and Reynolds (1997). The non-oriented powder was scanned from 2 to 70° 2θ with a step size of 0.009° 2θ, and a time per step of 0.5 s with a Bruker® D8-Advance Eco diffractometer (Cu Kα radiance, $\lambda = 1.5418$ Å, 40 KV, 25 mA) coupled with a Lynxeye Xe detector. The presence of a glass phase was deduced from the intensity of the diffraction band at 4.04 Å that corresponds to the total amorphous content (i.e. sum biogenic silica, volcanic glasses and organic matter) (Fagel et al., 2017).

The glass shard major element chemistry was analysed on the coarsest silty and sandy layer in 14 samples in LEs14 and 3 samples retrieved between 68 and 78 cm in LEs11. The glass shards were extracted following the protocol of Lowe (2011). An aliquot of bulk sediment samples (~0.8–2.4 g) was dry sieved at 80 µm. The <80 µm fraction was leached by adding 0.5 ml of concentrated acids HNO_3 14 N and HCl 6 N at 25°C for 15 min. The solid residue was rinsed three times by deionised water, dried at 40°C overnight before a liquid density separation. Bromoform was added to the dried residue for a 30 min. centrifugation at 4000 rpm. The tube was frozen dry by liquid nitrogen and the supernant was retrieved with acetone. The dried lighter fraction was mounted in epoxy resin for analysis by Electron Probe Micro-Analyser (EMPA) with a Cameca SX5 FE at the Rurh-University of Bochum (Germany). The analytical conditions were set at 15 kV and 8 nA with a beam size of 5–15 µm (more detailed analytical

protocol see Óladóttir et al., 2011). For calibration of the Kα X-ray lines, we used the following standards: albite (Al, Na), orthoclase (K), wollastonite (Si, Ca), TiO_2 (Ti), Fe_2O_3 (Fe), MgO (Mg) and Mn_3O_4 (Mn). Counting times were 10 s on peak and 5 s on background on either side of the peak. During analytical session the international glass standards A99 and VG2 were used as external standards to monitor the accuracy of the analyses and compare them with published values (Óladóttir et al., 2011). In the following text, the tephras are labelled as T1–T11 according to the stratigraphical order, T1 being the youngest layer.

For diatom analysis, sediment samples were taken at 2 cm intervals in LEs14 ($n=68$). A subsample of 0.5 g of sediment were treated with HCl and H_2O_2 to remove carbonate and organic matter, respectively. For microscopic analysis an aliquot of 4 µl was dried on a cover adding a mountant medium (Naphrax) on a microscope slide (Battarbee et al., 2001). A minimum count of 500 valves were carried out for each sample, except for diatom poor samples where only 100 valves were counted. Diatom were ide.epsied to species or genus level using the taxonomic references from Morales et al. (2014), Krammer and Lange-Bertalot (1986, 1988, 1991a, 1991b), Hartley et al. (1996) and Lange-Bertalot et al. (2000). To distinguish different association in the sediment core, a stratigraphically constrained sum-of-squares cluster analysis (CONISS) were performed with Tilia software (Grimm, 1991). Only diatoms with an abundance of >5% were plotted.

C/N ratio were measured at 1 cm sampling resolution for LEs11 ($n=69$) following the protocol of Hedges and Stern (1984). A few samples were also analysed in LEs14 ($n=23$) in order to compare their values with LEs11. The dried sediment sample was crushed by hand in a mortar and then treated with HCl to remove any carbonates. About 25–30 mg of sediment sample was analysed for C/N ratio at the Laboratory of Oceanology (Université de Liège, Belgium) with a Vario MicroCube elemental analyser coupled with a mass spectrometer Isoprime 100.

Complementary analyses of biogenic silica were measured by successive leaching procedures on ~50 mg of dried bulk sediment of LEs11 ($n=35$) at a sampling resolution of 2 cm, except in the coarsest layer (53–78 cm). The organic fraction was removed by addition of H_2O_2 10%, the carbonate fraction by HCl 1 N and then the total silica fraction by NaOH 0.2 N (Carter and Colman, 1994; Ohlendorf and Sturm, 2008). Al and Si contents were measured by Atomic Absorption using a spectrometer Analytikjena NovAA 300 (Department ARGENCO, Université de Liège) calibrated with artificial solution (50–200 mg/l for Si, 25 and 100 mg/l for Al). The detrital silica content is derived from a normative calculation (Leinen, 1977) using the measured Al content and the averaged Si/Al ratio (0.93) of four soil samples collected in the lake catchment. The estimated biogenic silica content corresponds to the measured total silica content minus the calculated detrital silica.

Core chronology

The ^{210}Pb, ^{226}Ra, ^{232}Th and ^{137}Cs data were measured with a 5 mm resolution in the upper 16 cm of core LEs13. The measurements were done with a low-background and high-efficiency gamma detector in the laboratory EPOC (Univ. Bordeaux, France). The ^{226}Ra content was removed from the ^{210}Pb content to calculate the excess ^{210}Pb activities (i.e. $^{210}Pb_{xs}$), further converted into age by using the Constant Flux/Constant Sedimentation model (CF/CS – Appleby and Oldfield, 1978). The peak of ^{137}Cs activity was used as independent chronological marker, where its maximum activity is recorded around 1965 (Stupar et al., 2014). Ages from ^{210}Pb chronology in LEs13 were correlated with LEs14 using the magnetic susceptibility profiles of both cores.

Radiocarbon dates were measured on bulk sediment or macroremain at the Gadam Laboratory from the Silesian Institute of Technology (Gliwice, Poland). Because ^{14}C dates can be affected by dissolved organic carbon derived from soils (Grimm et al., 2009), an age correction was applied to the bulk sediment according to Bertrand et al. (2012), who proposed to estimate the influence of organic matter input from the watershed on bulk radiocarbon ages using the measured atomic C/N ratios of lacustrine sediments. Defined from four lake sedimentary records from north Chilean Patagonia, such approach that allows to derive a reservoir age for bulk sediment is at least valid at the regional scale. The ^{14}C results were then calibrated using the Southern Hemisphere calibration curve (i.e. SHCal13 – Hogg et al., 2013). Dates from ^{210}Pb and ^{14}C were integrated in the age-depth model for LEs14 by Bayesian model using R software packages Bacon 2.5.3 (Blaauw et al., 2021). The followed methodology, even imperfect due to complex carbon cycle in volcanic lakes (Frugone-Alvarez et al., 2020), allow to estimate the age of the sedimentary record that will be further constrained by the tephrostratigraphy.

Statistical analysis

Multivariate analysis was performed on the XRF dataset using R software (R Development Core Team, 2018) and its *rgr* (Garrett, 2018) and *pcaPP* packages (Filzmoser et al., 2018). The geochemical data were centred log-ratio (clr) transformed prior to a Robust Principal Component Analysis (RPCA – Candès et al., 2011; Croux et al., 2013). This transformation is useful for this type of data, since it conserves all the elements, which facilitates the interpretation of the associated geochemical processes (Aitchison, 1986; Mueller and Grunsky, 2016). RPCA was chosen because it has been successfully applied on high resolution XRF data characterised by numerous outliers (Frugone-Alvarez et al., 2017; Żarczyński et al., 2019). Only the Principal Components (PC) with eigenvalues >1.0 were retained as significant for the total variance of the dataset (Davis, 2002).

To identify any climatic control, the geochemical ratios were compared to the precipitation data by a correlation matrix applied moving average filters of 3, 5 and 7 years for the period AD 1930–2014. The precipitation reanalysis data set of the CRU_TS 4.03 (Harris and Jones, 2020) were retrieved for an area comprised between latitude 45° and 45.5°S and longitude 72–72.5°W (http://climexp.knmi.nl). Prior, the CRU_TS data set was correlated with local (Villa Mañihuales) and regional (Puerto Aysen) instrumental precipitation data to validate the reanalysis data. May and June cumulated precipitation was used because it was the longest precipitation record to obtain a robust statistical analysis. The meteorological station of Villa Manihuales displays similar temporal trend with the regional station of Puerto Aysén (45°23′57.98″S, 72°40′37.99″W), giving for instance a Pearson correlation for accumulated May to June precipitation $r_{p\ MMJ}=.73$ $p<0.001$ (data Puerto Aysén 1960–2017 from INIA report – Hepp et al., 2018). The instrumental measurements of Villa Manihuales were then correlated with climate reconstruction CRU_TS 4.03 (Harris and Jones, 2020) in order to extend the calibration period to the whole 20th century ($r_{annual\ precipitation}=0.72$ $p<0.001$).

Changes in the diatom assemblage over time was evaluated by a Detrended Correspondence Analysis (DCA) (Hill and Gauch, 1980). Only the scores of the axis 1 were plotted against the diatom assemblages in order to study the species turnover between samples. This analysis was performed in the R software (R Development Core Team, 2018) using the vegan and rioja packages (Juggins, 2017; Oksanen et al., 2019).

Results

Sedimentology

Macroscopic observation, grain-size distribution and grey-scale levels allowed to identify three main sedimentological units in LEs14,

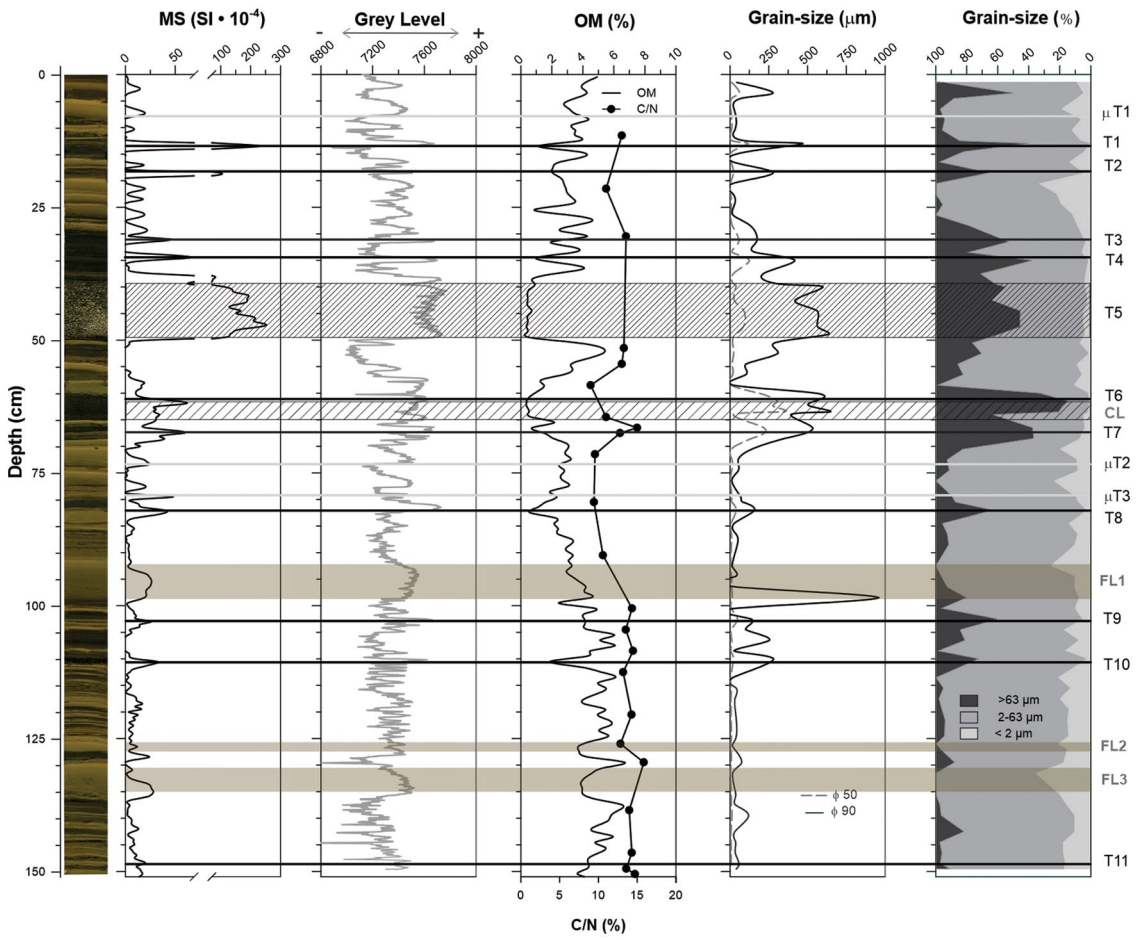

Figure 2. Detailed sedimentological description of core LEs14 based on physical parameters, that is magnetic susceptibility values (MS), SCOPIX grey-scale, organic matter content (from LOI550°C) and C/N ratio and grain-size parameters. The horizontal lines give the position of the tephras whereas the grey lines indicate microtephras. Coarse layer (CL) corresponds to the dashed interval. The three fine turbidites observed in the colour photograph are also reported (FL).

a detailed sedimentological description is given in Figure 2. The unit 1 (100–154 cm) is characterised by finely laminated light brown to dark brown organic-rich clayey silts (mean 10 μm, 78% 2–63 μm). A pluricentimetric homogeneous clayey interval with an upper lighter lamination is observed between 130.6 and 136 cm (reported as fine layer FL1 on Figure 2). A similar but thinner interval is also observed between 126.9 and 128.2 cm (FL2 on Figure 2). Unit 2 (60–100 cm) is made by diffuse laminations with similar silty grain size (mean 13 μm with 74% 2–63 μm) but lighter in colour than unit 1. An homogeneous clayey layer is evidenced between 92.3 and 98.3 cm (reported as FL3 on Figure 2). In the upper part of unit 2, a darker sandy interval (coarse layer CL on Figure 2) is evidenced between 60 and 65 cm, with 82% ±2.8 of sand. Its high ϕ50 value (228 μm ±129 – see data on Figure 2) contrasts with the ϕ50 values of the other coarse layers, recording an abundant fraction of medium sand (45 ±3% of 250–500 μm fraction). Unit 3 (0–60 cm) displays coarse millimetric to centimetric laminations between yellowish brown to dark brown clayey silts (mean 42 μm, 63% 2–63 μm). It contains a coarser light grey to dark grey layer between 39.5 and 49.5 cm composed of angular particles of various sizes (mean 31 μm, 49% 2–63 μm, ϕ50 55 μm ±31). This layer (labelled as T5) is overlaid between 29.6 and 39.5 cm by darker and diffusely laminated coarse silts to sands (mean 38 μm, 56% 2–63 μm%, and 39% >63 μm, ϕ50 39 μm ±41).

In addition to the darker layers at 39.5–49.5 cm (labelled T5, see below) and at 60–65 cm (CL), the sedimentation of core LEs14 is interrupted by 10 dark grey plurimillimetric fine sands observed at 13.2–13.5, 18.2–18.4, 31.5–31.7, 34.8–35, 60.7–61, 67.8–68, 81.9–82.3, 102.6–102.9, 110.7–111 and 148.6–148.8 cm (Figure 2). Those sandy layers (27–85 >63 μm, 159 μm ⩽ ϕ90 ⩽ 546 μm) were characterised by higher value in magnetic susceptibility by comparison to the background value and were interpreted as tephra layers. The two homogeneous pluricentimetric clayey layers FL1 and FL3 were interpreted as fine turbidite deposits, a sedimentation process often observed in the deepest area of lake, in particular in Chile (e.g. Moernaut et al., 2014; Van Daele et al., 2015). The thinner layer FL2 is probably also associated to a similar process.

The bulk mineralogy (Figure 3) is composed by both crystallised and amorphous phases. The main minerals are clay minerals (29% ±18), quartz (16% ±11), plagioclase (25% ±16) and pyroxene (3.4% ±1.7). Amphibole (<1%) and olivine (<6%) are also detected in some samples. The sum of amorphous phases reaches ⩾50% in the coarse interval 60–65 cm whereas it represents only 1% at 66–67 cm. Amorphous phase is made by at least 80% of volcanic glasses in the layers identified as tephra. Unit 1 is on average composed by detrital-derived components with 39% of clays, 21% of quartz and 5% of organic matter. The mean abundance of volcanic glasses (12%) and plagioclase (19%) is less abundant than in the lower units. Unit 2 is enriched in both volcanic glasses (30%) and plagioclase (28%) but depleted in clays (22%) and quartz (13). Unit 3 displays an averaged composition close to Unit 2, with more clay minerals (27%) and lower volcanic glasses (24%).

SEM imaging of the samples together with EPMA analyses confirms the presence of numerous volcanic shards. Figure 4 presents the average SiO_2 vs K_2O compositions of the glass shards along with their standard deviations (data in Table 1). Major composition of studied samples overpasses a wide range

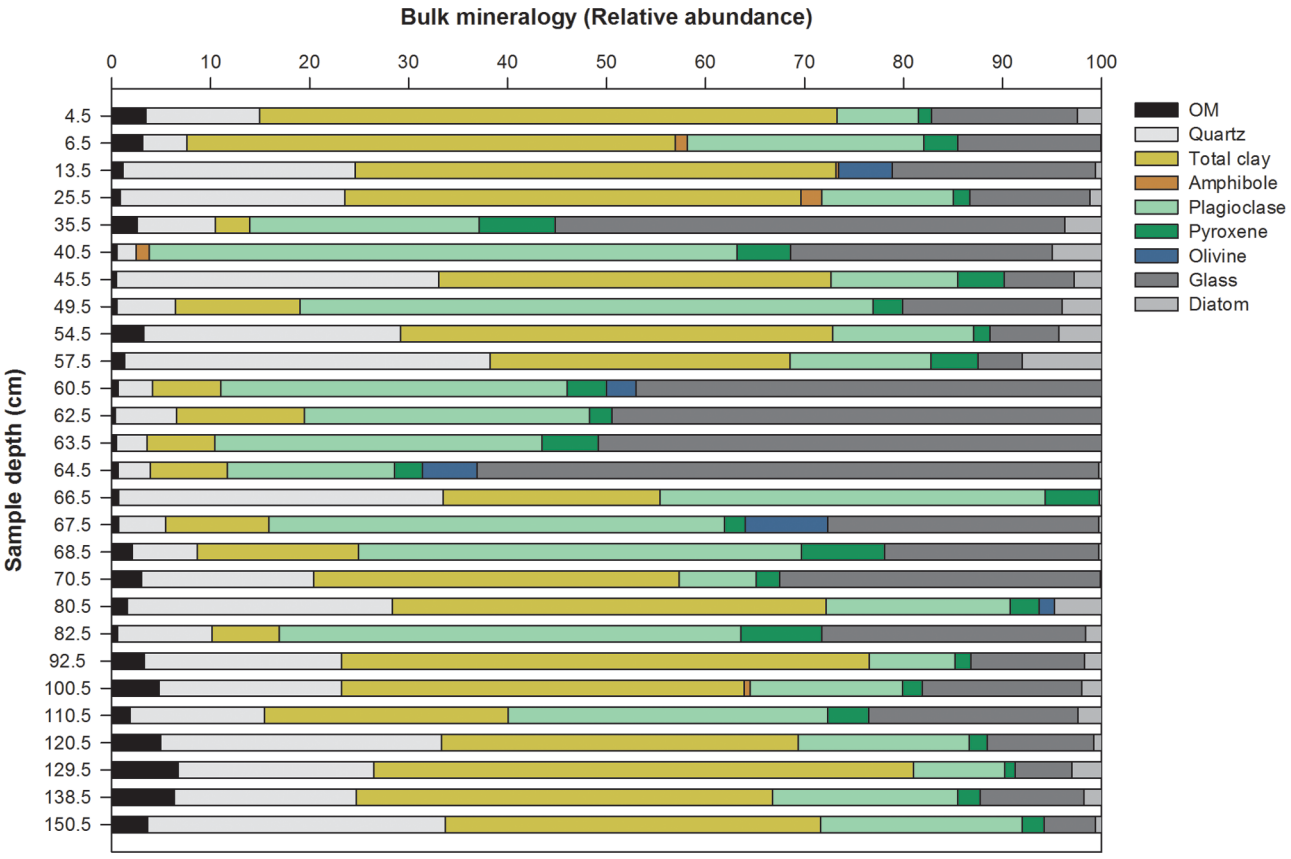

Figure 3. Bulk mineralogy of LEs14 ide.epsied by X-ray diffraction on bulk sediment powder (relative abundance).

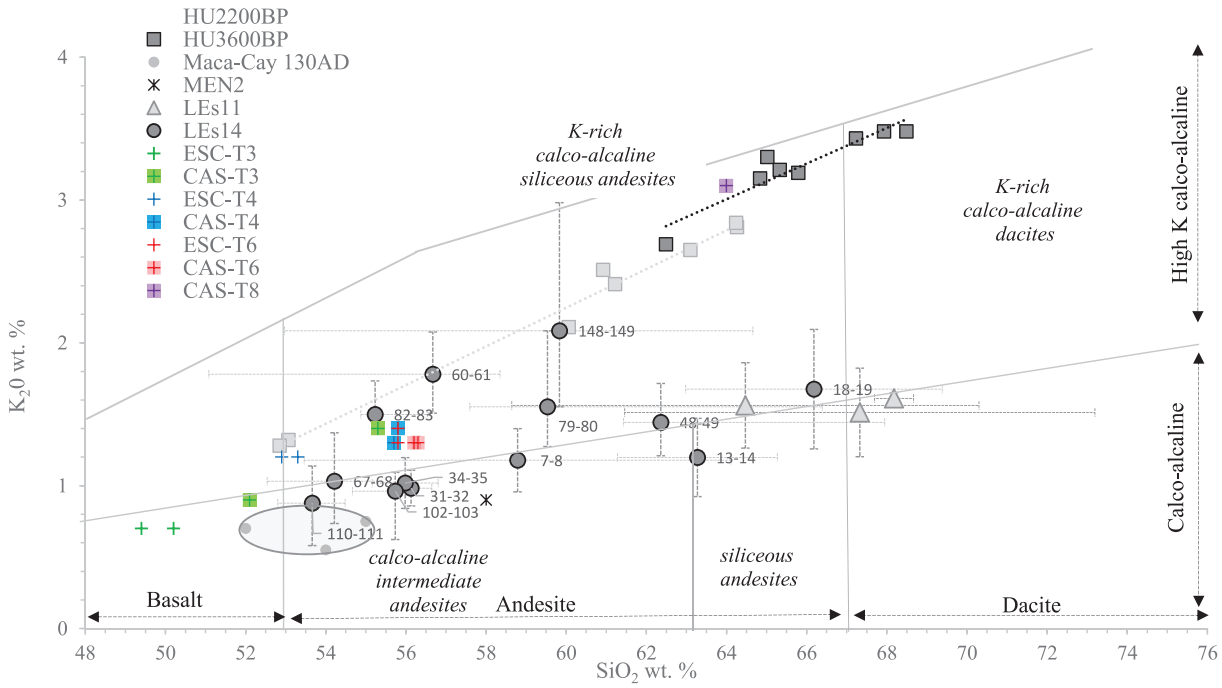

Figure 4. Averaged major element composition of tephra glass shard samples measured by microprobe and 1σ standard deviation (shaded lines). Data in Table 1. The chemical samples from Chilean Southern Volcanic Zone have previously been termed High, Low and Very Low Abundance magma types (Hickey et al., 1986; Hickey-Vargas et al., 1989, 2002; López-Escobar et al., 1993, 1995a, 1995b; Sellés et al., 2004; Watt et al., 2013). Analyses from historical (MEN1710 - Siebert et al., 2010) and prehistorical eruptions (i.e. MAC 1, HU2200 and HU3600 – Naranjo and Stern, 2004; Maca-Cay 130 AD – Mella et al., 2012) from regional volcanoes are reported for comparison as well as the measured composition of tephra samples retrieved in North Patagonian lacustrine sediments from Lakes Escondida and Castor (Elbert et al., 2013).

of silica content from basalts to dacites. Most samples range from intermediate calc-alkaline to K-rich siliceous andesites. The average compositions of the decimetric tephras observed in both cores LEs11 (53–78 cm) and LEs14 (39.5–49.5 cm, labelled as T5) are relatively similar and correspond to calc-alkaline intermediate andesite to siliceous andesites. The average composition of the glass shards ($n=27$) measured in three samples from LEs11 (i.e. 67–68, 73–74 and 77–78 cm) is 66.21 ± 5.38%

Table 1. Microprobe data on glass shards from core LEs14 and three samples retrieved from the main tephra layer in LEs11. Mean data are reported ±1σ.

Core	Sample	Tephra	nb.	SiO_2	TiO_2	Al_2O_3	FeO	MnO	MgO	CaO	Na_2O	K_2O	P_2O_5	Sum
LEs14	7-8	μT1	6	58.79 ± 5.33	1.14 ± 0.27	16.38 ± 1.78	6.73 ± 0.99	0.16 ± 0.03	2.63 ± 0.93	6.53 ± 2.39	4.24 ± 0.37	1.18 ± 0.22	0.54 ± 0.15	98.32
	13-14	T1	11	63.27 ± 1.99	0.89 ± 0.22	16.22 ± 1.16	4.44 ± 1.19	0.15 ± 0.05	1.60 ± 0.91	4.75 ± 0.99	5.21 ± 0.46	1.20 ± 0.27	0.41 ± 0.10	98.15
	18-19	T2	9	66.18 ± 3.20	0.78 ± 0.13	15.33 ± 1.46	4.15 ± 0.74	0.13 ± 0.05	1.24 ± 0.39	3.43 ± 1.02	4.53 ± 0.41	1.68 ± 0.42	0.24 ± 0.09	97.70
	31-32	T3	11	56.13 ± 0.2	1.68 ± 0.26	14.49 ± 1.35	10.97 ± 1.03	0.21 ± 0.03	3.30 ± 0.44	6.66 ± 0.36	3.88 ± 0.43	0.98 ± 0.13	0.27 ± 0.08	98.58
	34-35	T4	10	55.98 ± 0.82	1.63 ± 0.20	14.62 ± 0.83	11.03 ± 1.10	0.21 ± 0.03	3.49 ± 0.37	6.78 ± 0.42	3.73 ± 0.47	1.02 ± 0.18	0.28 ± 0.04	98.78
	48-49	T5	11	62.36 ± 5.59	1.33 ± 0.78	14.39 ± 1.23	7.95 ± 4.39	0.32 ± 0.35	1.88 ± 0.82	4.59 ± 1.61	4.09 ± 0.46	1.44 ± 0.27	0.25 ± 0.16	98.57
	60-61	T6	14	55.44 ± 1.94	1.65 ± 0.24	15.15 ± 1.2	8.68 ± 0.84	0.18 ± 0.04	3.60 ± 0.88	7.14 ± 0.73	4.39 ± 0.38	1.41 ± 0.28	0.61 ± 0.11	98.27
	67-68	T7	14	54.22 ± 1.70	1.46 ± 0.14	14.41 ± 0.91	10.04 ± 1.24	0.20 ± 0.03	4.98 ± 0.75	8.27 ± 0.81	3.65 ± 0.45	1.03 ± 0.34	0.33 ± 0.13	98.59
	73-74	μT2	14	56.45 ± 0.86	1.85 ± 0.39	14.98 ± 1.17	8.88 ± 1.28	0.19 ± 0.03	2.85 ± 0.41	5.95 ± 0.48	4.37 ± 0.24	1.98 ± 0.30	0.76 ± 0.19	98.28
	79-80	μT3	14	59.53 ± 6.86	1.30 ± 0.45	15.15 ± 0.99	7.62 ± 3.01	0.17 ± 0.06	2.88 ± 1.41	5.69 ± 2.11	4.14 ± 0.37	1.55 ± 0.53	0.33 ± 0.19	98.36
	82-83	T8	14	55.23 ± 1.31	1.80 ± 0.34	14.96 ± 1.05	9.31 ± 1.74	0.18 ± 0.04	3.32 ± 0.34	6.78 ± 0.63	4.26 ± 0.39	1.50 ± 0.24	0.65 ± 0.14	97.99
	102-103	T9	15	55.73 ± 0.50	1.70 ± 0.14	13.87 ± 0.64	11.49 ± 0.77	0.22 ± 0.04	3.88 ± 0.31	7.47 ± 0.38	3.38 ± 0.31	0.96 ± 0.13	0.25 ± 0.04	98.96
	110-111	T10	12	53.66 ± 0.82	1.87 ± 0.16	13.03 ± 0.36	12.61 ± 1.13	0.23 ± 0.03	4.53 ± 0.80	8.43 ± 1.32	3.27 ± 0.34	0.88 ± 0.26	0.39 ± 0.14	98.90
	148-149	T11	9	59.83 ± 4.83	1.39 ± 0.29	15.42 ± 0.80	7.17 ± 3.38	0.19 ± 0.03	2.33 ± 1.31	5.04 ± 2.86	4.81 ± 0.94	2.08 ± 0.90	0.32 ± 0.04	98.58
LEs11	68-69	T	10	67.32 ± 5.87	0.80 ± 0.58	14.26 ± 1.08	4.85 ± 3.48	0.15 ± 0.05	1.41 ± 1.08	3.83 ± 1.54	4.29 ± 0.54	1.51 ± 0.31	0.14 ± 0.11	98.56
	73-74	T	5	68.20 ± 0.49	0.58 ± 0.04	15.37 ± 0.50	3.23 ± 0.14	0.14 ± 0.03	0.76 ± 0.13	3.06 ± 0.07	4.79 ± 0.09	1.61 ± 0.04	0.14 ± 0.05	97.84
	77-78	T	12	64.47 ± 5.83	1.19 ± 0.58	14.25 ± 3.8	6.80 ± 3.44	0.17 ± 0.06	1.67 ± 1.08	4.26 ± 1.65	4.01 ± 0.51	1.56 ± 0.30	0.23 ± 0.10	98.63
	68-78	ave.	27	66.21 ± 5.38	0.93 ± 0.58	14.46 ± 1.12	5.41 ± 3.48	0.16 ± 0.05	1.41 ± 1.09	3.88 ± 1.53	4.26 ± 0.56	1.55 ± 0.27	0.18 ± 0.11	98.45

of SiO_2 and 1.55 ± 1.27% of K_2O. The silica content of the sample LEs14 48–49 averages 63.0 ± 5.27% of SiO_2 and 1.49 ± 0.26% of K_2O ($n = 11$).

In LEs14, the other plurimillimetric tephra layers are clustered in two main groups (K-rich group and K-poor group) according to their potassium content (Figure 4). (1) Within the K-rich group, sample 148–149 (T11) displays the highest K_2O values (2.5–2.7%) and plots within the field of K-rich calc-alkaline siliceous andesite. Sample 60–61 (T6) shows the largest chemical variability in the field of andesites (SiO_2 55.44 ± 1.94%, K_2O 1.41 ± 0.28%). The sample 82–83 (T8) falls within the fields of basalt to basaltic andesite with an average K_2O content of 1.50 ± 0.24% for 55.23 ± 1.31% of SiO_2. (2) Within the K-poor group, samples 31–32 (T3), 34–35 (T4), 102–103 (T9) and 110–111 cm (T10) display a narrow range of silica-poor glasses (53–56%) with ⩽1.2% of K_2O, that is all plotting into the field of intermediate andesite. The composition of samples 13–14 (T1) is clustered within the field of siliceous andesites with 1.2 ± 0.27% of K_2O whereas sample 18–19 (T2) is more scattered from andesite to dacite with 1.68 ± 0.42% of K_2O for 66.2 ± 3.2% of SiO_2. Sample 67–68 (T7) plots at the limit between calc-alkaline intermediate andesite and K-rich calc-alkaline siliceous andesite (SiO_2 66.2 ± 3.2%, K_2O 1.03 ± 0.34%).

The measured C/N (%) ratios are close in LEs11 and in LEs14 with a mean value of 12.7 ± 1.4 and 12.84 ± 1.86, respectively. A pronounced peak in C/N (15) is observed at 66–67 cm in LEs14, below the coarse layer interval (CL, Figure 2). The averaged organic matter content was estimated at 3.3 ± 1.6% by LOI in LEs14, with the highest values measured in unit 1 (4.8 ± 0.4%) and the lowest values (0.6 ± 0.4%) in the coarse layer (Figure 2). Note LOI-deduced organic matter values were lower than the estimations based on the abundance of carbon measured by optical Mass Spectrometry. Assuming 50% of carbon in organic matter, the averaged organic matter content in LEs14 evolves from 7.9 ± 3.6% in unit 1,and 3.8 ± 2.3% in unit 2 to 8.8 ± 5.7% in unit 3 (core average 7.11 ± 4.1), the highest value (13.2%) being observed at 30–31 cm.

Core chronology

The age model of core LEs14 is reported on Figure 5. It integrates the surface age, ^{210}Pb ages estimates from CF/CS model in LEs13 and three calibrated and reservoir-corrected ^{14}C dates from LEs14 (Table 2). The 11 tephras layers (T1–T11) and the three homogeneous clayey layers capped by a thin lighter layer (FL1–FL3) were considered as instantaneous deposits in the Bacon age model.

For the upper core section, the ^{137}Cs data confirm the $^{210}Pb_{xs}$ age model (Figure 5a). The maximum ^{137}Cs activity (42 mBq/g) observed at 4.5 cm in LEs13 corresponds to an age of 1965 ± 6.5 year AD according to the CF/CS $^{210}Pb_{xs}$ age, that is an age consistent with the highest period of nuclear tests in the Pacific Ocean (Stupar et al., 2014). While in the lower core section, two over the four calibrated ^{14}C ages were used, because the sample 104–105 cm and 151–152 cm were considered as outliers (Figure 5b). Even after a correction of the reservoir effect derived from C/N ratio, there is still a significant difference with the closest age-control point at 107–108 cm obtained from a macroremain (wood fragment). This observation suggests that the reservoir correction applied on bulk sediment is not sufficient due to high supplies of old carbon from the watershed of old organic matter in the lower part of LEs14 (average C/N ratio ~15 for the lower core section – see Figure 2). Figure 5b compares two age models, with and without considering in account the two ^{14}C ages obtained on bulk sediment at 104.5 and 152.5 cm. Without considering the ages measured on bulk sediments, the Bacon age-depth model indicates that core LEs14 covers ~ 3.5 kyr within 154 cm, with an averaged sedimentation rate of ~0.4 mm/year, reaching up to 0.6 mm/year for the upper 10 cm. This age model is consistent with the interval cover by LEs11 estimated from one ^{14}C date measured on a bivalve shell (Diplodon chilensis) retrieved between 84 and 86 cm (Table 2). Not including the three coarse intervals at 11–11.5, 15–16 and 53–78 cm considered as tephra deposition the calibrated age of 113–235 AD suggests an averaged sedimentation rate of 0.4 mm/year. By extrapolating this sedimentation rate, LEs11 encompasses ~2 kyr within 94 cm. Such age supports the youngest sequence covered by LEs14 based on the correlation between the two cores LEs11 and LEs14. Note this age model will be further supported by tephrostratigraphy (see Section 5.2).

Biogenic silica and diatoms assemblages

Microscope counting in LEs14 evidences an overall low diatom abundance in Lake Esponja, confirmed by the low biogenic silica content of 5 ± 3% estimated by leaching method in LEs11 (data reported on Supplemental Material Figure 1, available online). Nevertheless, LEs14 is characterised by an important diversity in the benthic diatoms with 23 genus and 153 species whereas only two genera of planktonic diatoms were observed.

The DCA results indicated three principal periods of the diatom assemblage: DZ1 (150–80 cm; 1.4 kyr BC–200 BC), DZ2 (80–55 cm; 200 BC–316 AD) and DZ3 between 55 and 0 cm (~316 AD–present), subzones inside of these was defined by CONISS and shown in Figure 6. The main change observed in DCA was associated with the replacement of planktonic and tycoplanktonic diatoms, such as Cyclotella sp, Aulacoseira spp and Staurosira construens, to benthic diatoms such as Frustulia sp and Surirella sp (Figure 6).

The DZ1 was dominated by planktonic species (i.e. Aulacoseira and Cyclotella) and tycoplanktonic genera (Staurosira) with low relative abundance (<20%) of benthic genera (i.e. Surirella, Gomphonema, Cymbella and Stauroneis). The planktonic taxa were progressively replaced by two benthic genera Frustulia and Surirella in a transition interval (DZ1b 100–80 cm). The intermediate interval (DZ2 80–55 cm) showed low taxa richness ($n = 31 \pm 46$) and was dominated by benthic genera, such as Surirella (<80%), Cymbella and Eunotia, the latter with relative abundances of less than 20%. A few planktonic diatoms Aulacoseira were observed in one sample (62–65 cm) retrieved in the coarse sandy layer CL (60–65 cm). DZ3 zone (55–0 cm) was characterised at the base by a tephra deposit (Tephra 5). This volcanic activity caused a slight change in the relative abundance of the taxa but it did not affect the taxonomic composition of the assemblage. The diatom assemblages of DZ3 was dominated by the benthic genera Frustulia (⩽60%) and Surirella (20–80%). The planktonic Aulacoseira was also well represented (<40%), but with percentages remaining variable throughout the zone. DZ3 was also characterised by diverse benthic taxa than were minor represented or absent in the DZ1 and DZ2 zones including Eunotia, Stauroneis, Cymbopleura, Gomphonema and *Stenopterobia*. This was observed especially in the upper 25 cm.

Sediment geochemistry

The RPCA was performed on 12 elements since Mn, Y and Ba registered insignificant communalities <0.5. The first two PC were highly significant with a cumulated variance of 88.56% (PC1 56.7%, PC2 31.86%). In the PC1-PC2 biplot diagram (Supplemental Material Figure 2, available online), the elements were clustered in three groups (see the correlation matrix given as Supplemental Material Figure 3, available online). Al, Si, K and Rb (group 1) plot along positive PC1 axis whereas Ti, Ca, Sr and Zr (group 2) and Mn, Fe, Zn, S and Br (group 3) were rather aligned along the PC2 axis with negative or positive value, respectively.

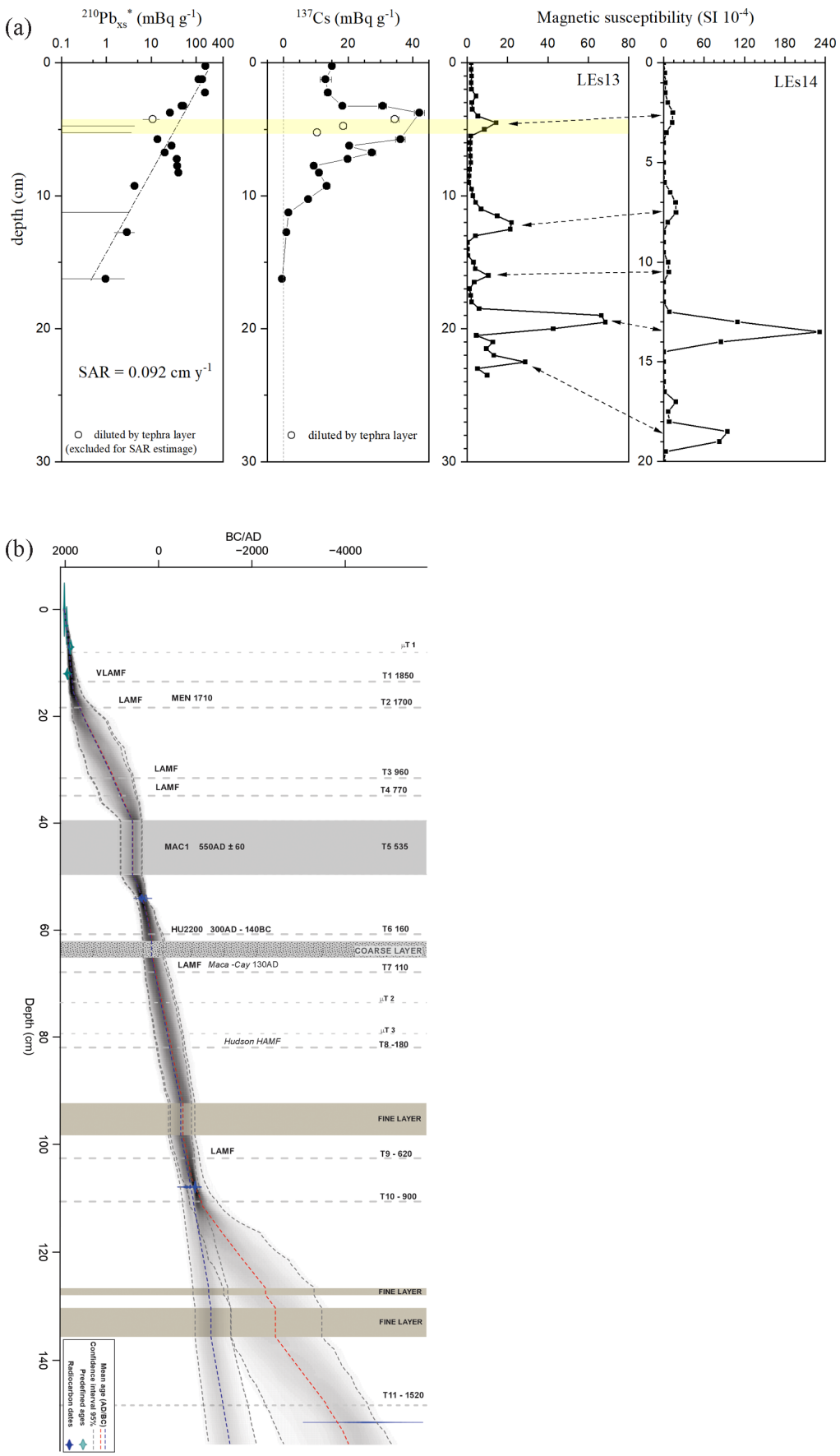

Figure 5. (a) Age model for the upper part of core LEs14 based on ^{210}Pb and ^{137}Cs data measured on LEs13 and transferred by correlation with magnetic susceptibility to LEs14. (b) Age model for the lower part of core LEs14 derived from ^{14}C data reported on Table 2. The horizontal dashed lines correspond to the main tephra layers that have been considered as event deposits (i.e. without any time). Two age models are compared, with (red line) and without (blue line) considering in account the two ^{14}C ages obtained on bulk sediment at 104.5 and 152.5 cm. Without considering the ages measured on bulk sediments, the Bacon age-depth model indicates that core LEs14 covers 3.5 kyr within 154 cm, with an averaged sedimentation rate of ~0.4 mm/year, reaching up to 0.6 mm/year for the upper 10 cm. This age model is consistent with the interval cover by LEs11 estimated from one ^{14}C date measured on a bivalve shell (Diplodon chilensis) retrieved between 84 and 86 cm (Table 2).

Table 2. AMS ^{14}C ages from macroremains and bulk sediment of cores LEs11 and LEs14.

Lab. nb.	Core	Sample interval cm	Sample type	Age ^{14}C BP	Range of calendar (calibrated) age 95% confidence level	Organic matter %	C/N %	Reservoir correction year
GdA-3407	LEs11	84–86	Macroremain (bivalve)	1890 ± 25	86 AD (1.1%) 93 AD 113 AD (94.3%) 235 AD			0
GdA-4034	LEs14	53–54	Bulk sediment	1760 ± 24	1704 BP (95.4%) 1570 BP	13.3	13.0	6
GdA-4035	LEs14	104–105	Bulk sediment	3760 ± 30	4220 BP (1.1%) 4208 BP 4156 BP (92.6%) 3966 BP 3945 BP (1.6%) 3930 BP	6.5	13.5	340
GdA-4036	LEs14	107–108	Macroremain (charcoal)	2630 ± 26	2773 BP (83.7%) 2698 BP 2633 BP (3.5%) 2616 BP 2589 BP (7.1%) 2537 BP 2528 BP (1.1%) 2516 BP			0
GdA-4037	LEs14	151–152	Bulk sediment	6108 ± 33	7147 BP (2.2%) 7127 BP 7015 BP (93.2%) 6792 BP	10.0	15.8	1140

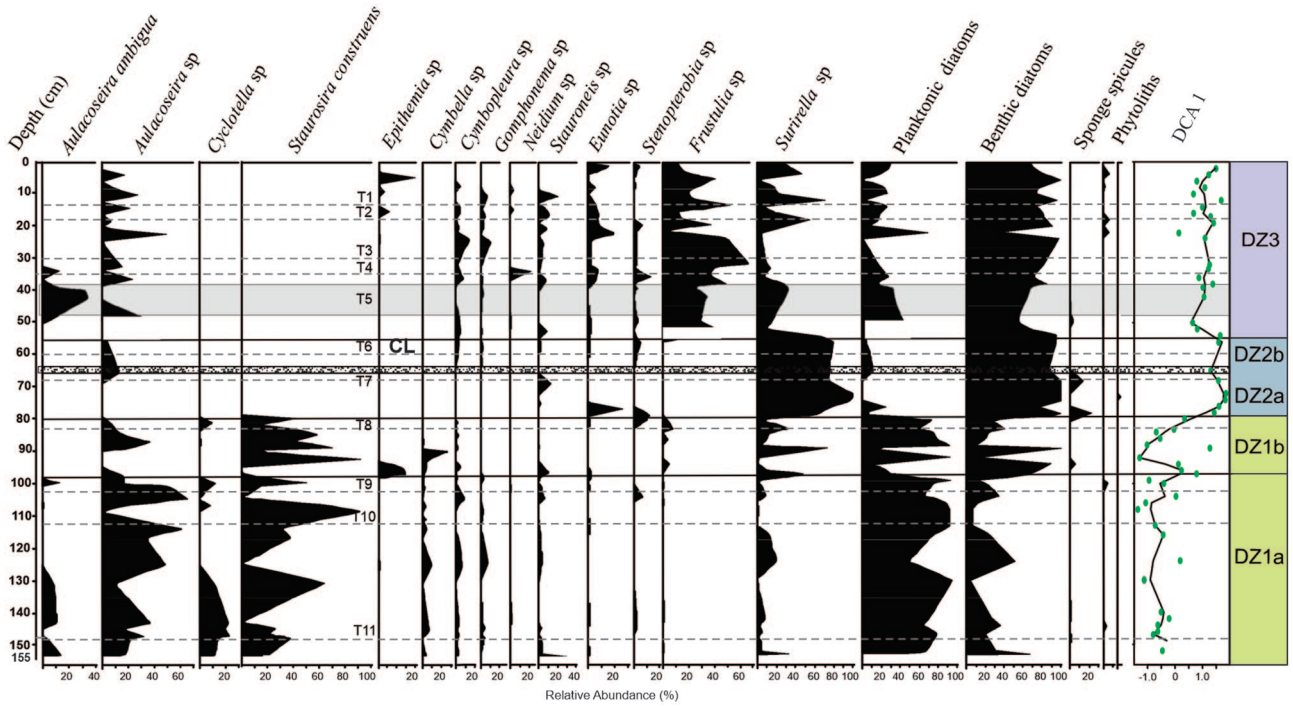

Figure 6. Diatom assemblages and zonations observed on LEs14.

Discussion

The section is divided into three sub-sections. (1) The multivariate PCA analysis will allow to identify the different types of sedimentary components that settle down at the bottom of the Lake Esponja. (2) Chemical microprobe and SEM/EDS analyses of glass shards will be used to confirm the presence of tephra layers in its sedimentary record and to correlate them to past known eruptions of the regional volcanoes and lacustrine tephra records. (3) Combined with the geochemical data, the diatom assemblages will be interpreted in terms of water column conditions in relation to local or regional perturbations in the watershed induced by either volcanic, tectonic or climate changes. An overall reconstruction of the paleoenvironmental evolution of Lake Esponja setting will be proposed for the last 3.5 millennia based from both geochemical and biological proxies.

Identification of sedimentary components

The RPCA analysis applied on the geochemical sedimentary composition of Lake Esponja evidences marked changes in the sedimentary supplies in relationship with detrital and volcanic inputs. The analysed geochemical elements were clustered in three groups in the binary PC1-PC2 diagram (Supplemental Material Figure 2, available online). The RPCA correlation matrix on XRF core scanner dataset of core LEs14 is given on Supplemental Material Figure 3, available online.

In the first group aligned along PC1 axis, the Pearson correlation between Rb and K (r=.72 - Supplemental Material Figure 3, available online) indicates a control by fine detrital supplies enriched in clay minerals and K-feldspars (Kylander et al., 2011). Likely, the correlation between Al and Si (r=0.92 – Supplemental Material Figure 3, available online) evidences a dominant detrital origin for Si, consistent with the low abundance of diatoms in the sediment.

Among the group 2 the relationship between Ca and Sr (r=0.87 – Supplemental Material Figure 3, available online) is indicative of the presence of plagioclase, that is the dominant mineral observed in the tephra layers. Zr that is correlated to Sr (r=0.53 – Supplemental Material Figure 3, available online) and Ti (r=0.50 – Supplemental Material Figure 3, available online) is

often related to coarse-grained fractions (Kylander et al., 2011) and/or to volcanic assemblages (Davies et al., 2015).

In the group 3, the highest correlation was observed between Br and S ($r=0.80$ – Supplemental Material Figure 3, available online) and S and Zn ($r=0.73$ – Supplemental Material Figure 3, available online). As those elements are often related to organic matter content (Ziegler et al., 2008), the group 3 mainly represents the supplies of allochthonous organic matter by physical weathering and erosion in the watershed. PC1 is therefore indicative of fine detrital supplies whereas the PC2 rather correspond to coarser supplies.

Identification of volcanic supplies

Quaternary volcanoes of SVZ show a close relationship with NE-striking tension cracks and with WNW striking basement faults of the Liquiñe-Ofqui system (e.g. Cembrano and Lara, 2009). The Lake Esponja is located at ~70 km East of volcanoes Cay and Macá, 120 km SE of volcano Mentolat, 134 km SSE of volcano Melimoyu and ~70 km NE of volcano Hudson. The lake may be affected by pyroclastic falls mainly from Cay or Macá (>10 cm) and from Mentolat (~10 cm) and in a lesser way by Hudson (<10 cm) (SERNAGEOMIN, 2012; Watt et al., 2013). The stratovolcano Cay (45°03′S, 72°59′W, 2090 masl), is of one of the large composite central volcanoes in SVZ, (i.e. the closest of Lake Esponja) probably still active but it has no record of past eruptions (Naranjo and Stern, 2004). The Macá volcano is a large active stratovolcano (45°06′S, 73°10′W, 2960 masl) with only one known post glacial explosive eruption MAC1 at 550 ± 60 AD (Naranjo and Stern, 2004). The Mentolat volcano (47°42′S, 73°04′W, 1660 masl) had one eruption MEN1 at 5.5 ka BC (Naranjo and Stern, 2004; Watt et al., 2013). The Melimoyu volcano (44°08′S, 72°88′W, 2400 masl) is a large volcano covered by a glacier that had two major known eruptions, that is MEL1 at ~880 BC year and MEL2 at ~330 AD year (Naranjo and Stern, 2004; Watt et al., 2013). However, its eastern tephra dispersion rules out any influence on Lake Esponja (Weller et al., 2014). The active basaltic-dacitic volcano Hudson (45°54′S, 72°58′W, 1905 masl) has two prehistorical eruptions ca. 1875 ka ±235 BC (H2 3.6 ^{14}C kyr BP, Naranjo and Stern, 2004) and ~ 5.8 ka BC (H1 7.43 ^{14}C kyr BP – Naranjo and Stern, 1998; Watt et al., 2013).

SVZ volcanoes fall into three chemical groups, reported in Stern et al. (2015), distinguished by their different concentrations of the incompatible elements like K_2O (Figure 4). Hudson and Melimoyu volcanoes are characterised by High Abundance magma (HAMF – Kratzmann et al., 2010; López-Escobar et al., 1993, 1995a; Naranjo and Stern, 1998, 2004) while Maca, Cay and Yanteles stratovolcanoes are Low Abundance volcanoes (LAMF – D'Orazio et al., 2003; Gutiérrez et al., 2005; López-Escobar et al., 1993, 1995a, 1995b). The Mentolat volcano falls in the field of Very Low magmatic Field (VLMF) with lower K_2O content at any given content SiO_2 (López-Escobar et al., 1993; Naranjo and Stern, 2004; Watt et al., 2013). Very Low Abundance centres are characterised by the presence of amphibole in their eruptive products (López-Escobar et al., 1993, 1995a, 1995b; Sellés et al., 2004; Watt et al., 2013).

The age of each tephra layer identified in the sedimentary records of LEs14 has been deduced from the age model to identify any correlation with the known Holocene eruptions of the surrounding volcanoes (Table 3). The main decimetric tephra layer observed in LEs14 is attributed to the Macá eruption MAC1 according to both its age and chemical composition. In LEs14, the age model suggests a median age of 537 AD (357–814 AD) for the main tephra layer T5. This age is consistent with the youngest age of the Macá volcano eruption MAC1 dated at 550 ± 60 AD (Naranjo and Stern, 2004). Moreover, the chemical composition of the glass shards retrieved from this main tephra layer in both cores

Table 3. Tephra characterisations and correlation to known regional eruptions.

Tephra ID	Depth interval (cm)		Age model				Glass major chemistry	Magma field	Volcanic eruptions					
			Min	Max	Median	Mean			Source	Name	Min	Max	Mean	Age ^{14}C BP
			AD/BC								Year AD/BC			
µT1	7.8	8.0	1859	1943	1906	1904	interm. andesite	LAMF						
T1	13.2	13.5	1720	1915	1852	1843	sil. andesite	VL-LAMF	Mentolat					
T2	18.2	18.4	1412	1857	1699	1682	K-rich sil. andesite	LAMF	Mentolat	Men1710[1]	1710			
T3	31.5	31.7	563	1436	957	968	interm. andesite	LAMF	Maca					
T4	34.8	35.0	482	1268	780	803	interm. andesite	LAMF	Maca					
T5	39.5	49.5	357	814	537	552	K-rich sil. andesite	LAMF	Maca	MAC1[2]	610	490	550 ± 60	
T6	60.7	61.0	−65	345	178	168	K-rich andesite	HAMF	Hudson	HU2200[2]	300	−140	250	2200
T7	67.8	68.0	−183	283	82	74	interm. to sil. andesite	LAMF	Maca	Maca130[3]			130	
µT3	79.3	79.4	−498	96	−185	−190	K-rich sil. andesite	LAMF	?					
T8	81.9	82.3	−534	32	−246	−248	K-rich basaltic andesite	HAMF	Hudson	HU2200[2]	300	−140	−250	2200
T9	102.6	102.9	−779	−345	−587	−583	interm. andesite	HAMF	?					
T10	110.7	111.0	−961	−520	−785	−755	interm. andesite	LAMF	?					
T11	148.6	148.8	−1918	−969	−1373	−1387	K-rich sil. andesite	HAMF	Hudson	H2/T5[2]	−1640	−2110	−1875 ± 235	3600

The numbers in superscript indicate the references for the eruptions: (1) Siebert et al. (2010); (2) Naranjo and Stern (2004); (3) Energia Austral Ltda 2012 cited in Mella et al. (2012).

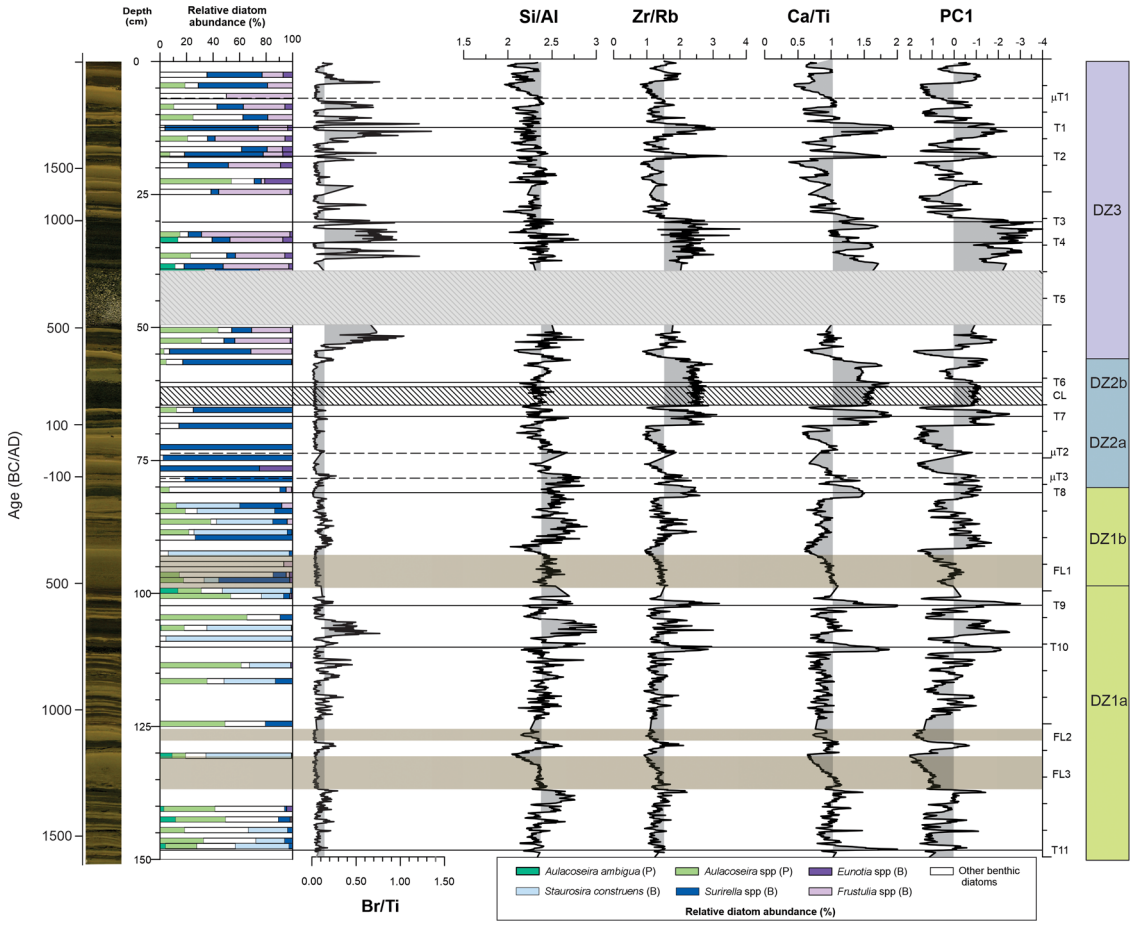

Figure 7. Paleoenvironmental synthesis of LEs14 data based on detailed diatom assemblage composition given at Figure 6 and XRF-core scanner data reported as elementary ratios and the first principal component PC1. XRF ratios are presented as ln(Si/Al), ln(Zr/Rb), ln(Br/Ti) and ln(Ca/Ti) indicating fine, coarse or organic-rich detrital matter or volcanic supplies, respectively. The letters reported on the right side of the figure correspond to peculiar layers identified in the core description, that is microtephras (μTx), tephras (T), fine turbiditic layers (FLx) and CL coarse layer (CL). The layers are labelled according to the stratigraphical order.

LEs14 and LEs11 fall within the field of Low Abundance Magma Field (LAMF), a chemical signature consistent with the few measured compositions of MAC1-related glass shards (Figure 4). The median age (~1699 AD) of tephra layer T2 (18.2–18.4 cm) is consistent with the historical eruption of the Mentolat volcano MEN1710 (Siebert et al., 2010). Such origin also agrees with its VLAMF to LAMF chemical signature (Figure 4). The age of deposition for tephra layer T6 estimated ca 168–178 AD (median-mean) is consistent Hudson HU2200 eruption (2.2 kyr ^{14}C, 300 AD–140 BC). This correlation is also supported by the HAMF-type chemical signature of T6 glass shards ranging in the field defined for the Hudson HU2200 eruption (Kratzmann et al., 2010; Naranjo and Stern, 2004) from basaltic to siliceous andesites (Figure 4). Likely the tephra layer T11 (median ~1373 BC) is also characterised by a Hudson-like signature (HAMF) within the field of K-rich siliceous andesites, consistent in particular with the Hudson H2/T5 eruption (HU3600 BP, 1875 ± 235 BC, Naranjo and Stern, 2004 – Figure 4).

The Lake Esponja sediments record additional tephra layers (Figure 4) that probably correspond to minor eruptions not reported in literature. The tephra layer T1 (13.2–13.5 cm, median 1852 AD) and T10 (median ~785 BC) display a K_2O-low geochemical signature in the LAMF. Their measured chemical signature is rather consistent with some Macá-related eruption. In addition, the tephra correlation for LEs14 may be compared with lacustrine tephra record in nearby lakes (Table 3). T5 (median 537 AD) is probably equivalent to the tephra deposition CAS-T3 and ESC-T3, respectively identified in Lake Castor and Lake Escondida (see location on Figure 1) at an extrapolated age of ~160 AD (Elbert et al., 2013). Weller et al. (2015) already proposed their correlation to MAC1 according to the glass shard chemistry of ESC-T3 that is different than any Hudson-related tephra as reported in Elbert et al. (2013). Likely T3 (median 957 AD) and T4 (median 780 AD) are correlated to the tephra deposition CAS-T1/ESC-T1 (950 AD) and CAS-T2/ESC-T2 (400 AD), respectively. Note these correlations, consistent in age for T3, are not supported by any chemical data for those tephra layers. T6 (median ~178 AD) and T8 (~246 BC) with their K-rich HAMF type composition may be lateral equivalents of the tephras CAS-T4/CAS-T4 (90 AD) and CAS-T6/CAS-T6 (310 BC). By stratigraphic interpolation T7 (median ~82 AD) would be related to CAS/T5/ESC-T5 (50 BC). T7 probably corresponds to a tephra observed in the Villa-Mañihuales area dated at 130 AD (Energia Austral Ltda 2012 cited in Mella et al., 2012) and associated to the volcanic complex Maca-Cay. Finally, the chemical signature of the oldest tephra observed in LES14 T11 is consistent with the K-rich and Si-rich composition of CAS-T8 that was correlated to Hudson H2/T5 eruption (Elbert et al., 2013). The correlation is supported by both the peculiar chemical signature of CAS-T8, even its median interpolated age (~1373 BC) is younger. The Hudson H2 tephra has also been recorded in the sediments of Lake Unco (see location in Figure 1, data from Weller et al., 2014).

Paleolacustrine and paleoenvironmental conditions

The evolution of the diatom assemblages in LEs14 is reported according to core depth respect to with PC1 and a selection of geochemical ratios (Figure 7). Si/Al, Zr/Rb, Br/Ti and Ca/Ti are used as proxies for fine, coarse or organic-rich detrital matter or volcanic supplies, respectively. The overall depth evolution of

benthic diatom assemblages in Lake Esponja, detailed in LEs14, evidences pronounced changes in the lake conditions (depth, turbidity, water chemistry) over the last ⩽3.5 kyr. Such environmental evolution mostly reflects the weathering intensity within the lake watershed, controlled by (1) tectonic and/or (2) climate-driven changes (Battarbee et al., 2001).

Tectonic control. The Ca/Ti and Zr/Rb curves display pronounced and sharp peaks that mostly coincide with the sedimentary tephra record. However, the presence of several tephra layers along the sediment core does not reflect significative changes in the diatom assemblage in LEs14 as observed for other Chilean lakes (e.g. Lake Galletué 38°S – Cruces et al., 2006; Laguna del Maule, 36°S – Carrevedo et al., 2015). Tephra deposition and their reworking in the catchment supplies a continuous addition of nutrients to the lake that sustains the lake productivity and in particular diatom growth. However, in Lake Esponja, this was only obvious in the main tephra T5, where the Aulacoseira–Surirella association (>40%) emphasises a marked increase in nutrients and less transparency than in previous stages. Besides, the presence of Aulacoseira ambigua inside the tephra indicates that this deposit was not enough to avoid its development, a behaviour that has been also observed in central Andes (Frugone-Alvarez et al., 2020).

The major change in diatom assemblage, that is the replacement of planktonic taxa by benthic ones (DZ3), was probably due to the closure of the Lake Esponja as a consequence of a major earthquake-induced rupture occurring along the Río Mañihuales Fault and regionaly related to LOFZ. This significative change occurred after a medium sand interval (CL) between 60.1 and 65.7 cm (63 BC–345 AD, best age 166 AD), characterised by relatively high Zr/Rb and Ca/Ti ratios, indicates a high detrital supply, characteristic of rapid sedimentation event related to watershed perturbation and further sediment remobilisation.

The age of this massive interval may be compared with a density-flow deposit (i.e. event SL-F) observed in the Aysén fjord sedimentation (Van Daele et al., 2013). Particularly, SL-F event was dated at ~30 BC/100 AD in Wils et al. (2018) and based on a probabilistic approach the interpretation of the seismic-reflection data gave evidence that this event occurred on the same fault as the 2007 earthquake (Vanneste et al., 2018). According to the same study, the prehistorical earthquakes of the Aysén Fjord most likely had a low to moderate magnitude <6.5 as expected for crustal earthquakes. The SL-F event was even larger with an estimated magnitude of 6.5 (Vanneste et al., 2018). The most likely ruptures are generally situated on the closest faults to the Aysen fjord, that is the Quitralco, Azul Tigre or Río Mañihuales Faults (Vanneste et al., 2018). According to the revised age model of Wils et al. (2020), SL-F event includes two partial earthquake ruptures occurring at AD~15 and AD~100, the oldest one affected the southern part of the Valdivia segment (i.e. the closest to Lake Esponja location) whereas the youngest one only ruptured along its northern segment. The purely detrital mineralogy of sample 66–67 cm (Figure 3) could record the inception of the massive event, its age being consistent with the major tectonic event SL-F (Wils et al., 2020) in Aysén fjord. The mineralogy of the coarse sandy interval 60–65.7 cm evidences the contribution from reworked tephra (T7) as observed in Aysén fjord (Van Daele et al., 2013).

Climate control. The geochemical ratios, and in particular Si/Al ratio, have been compared to CRU meteorological data to identify any climate control. For the 20th century, the evolution of Si/Al ratio in LEs14 displays a significant Pearson correlation (0.70, $p < 0.001$) with austral winter CRU precipitation data, the highest correlation being obtained with a 7-year average (Supplemental Material Figure 4, available online). The lowest Si/Al values ranging between 6 and 7 ca 1925, 1960 and 1990 AD are roughly consistent with the lowest winter precipitation (~135 mm). Likely the highest Si/Al values (8–10) coincide with the highest winter precipitation comprised between ~170 and 210 mm (ca 1905, 1940, 1968 and 1998 AD). The austral winter precipitations probably enhance weathering processes within the watershed leading to more surface runoff along the lake margins and remobilisation of the Quaternary alluvial formation along the margin. The remobilised particles may then be selectively transported according to grain size, the finest particles settling down in the farthest location. Such observation evidences that the fine detrital supplies, distributed along PC1 axis, are controlled by winter precipitation intensities. The Si/Al ratio may therefore be used in LEs record as a proxy for paleoprecipitation.

Along of the LEs14 record, the Si/Al ratio profile shows a slightly change at ~ 80–75 cm (200–90 BC). Before 80 cm (<200 BC) high Si/Al ratio values and high variability suggested high winter precipitation and a resulting increase of the lake level and turbid waters, possibly favoured with the connection of the river Mañihuales. The dominance and high variability of Aulacoseira and Staurosira confirm these lake conditions with water turbulence and coastal areas dominated by circumneutral to alkaline conditions in the context of a tendentially deep lake as observed in Laguna de Maule, central Chile (Carrevedo et al., 2015). This predominating wet period has been recognised in pollen sedimentary record from Lake Guanaco (Moreno et al., 2009) associated to an intensification of the SWW.

The Si/Al values decrease after 75 cm would be related to less winter precipitation and therefore a reduced water input from the river and/or the watershed. Calm water conditions were favourable expansion of benthic diatoms, mainly Surirella, a genus that lives in shallow environments with high silica requirement (Matteuzzo et al., 2015). The predominance of benthic diatoms in the assemblage for the upper part of the core (Figure 6), added to sedimentological changes (Figure 2), could corroborate a main tectonic control, with lesser climatic control reflected in discrete variations in the relative abundance of benthic diatoms and the sudden occurrence of Aulacoseira spp.

Environmental evolution. The punctual tectonic and climatic controls being identified in the LEs14 sedimentological and geochemical record, the overall interpretation of the three identified diatom zones is summarised in the next section.

(1) The lower part of LEs14 (i.e. diatom zone DZ1 154–80 cm, ~2 kyr BC–140 BC – Figure 6) was dominated by tycoplanktonic diatoms (i.e. Aulacoseira ambigua, Aulacoseira aff. ambigua, Staurosira construens) associated with ⩽5% of neutrophil diatoms (i.e. Cyclotella group), consistent with a pH-optimum of ~7–7.4 (Van de Vijver et al., 2002). The association of Aulacoseira, Cyclotella and Staurosira construens suggests eutrophic conditions in a relatively deep but turbid lake (Witak et al., 2017). The abrupt fluctuations in the abundance of Aulacoseira and Staurosira observed in DZ1a (100–154 cm, 600–2000 years BC) give place to an increase of epiphytic diatoms like Cymbella and Epithemia in the upper part of this interval (DZ1b 80–100 cm, ~200–520 BC). The main change in the diatom composition occurs in the transition interval between DZ1 and DZ2 (DZ1b) where the fragilarioid taxa Staurosira and Aulacoseira were replaced by Surirella taxa. Staurosira has been observed in shallow coastal habitats of deep lakes characterised by fairly long seasonal lake-ice cover (Fernández et al., 2013). Consistent with temperature optima in Canadian artic lakes fragilarioid group is present in cold summer air temperatures (Finkelstein and Gajewski, 2008). Aulacoseira kept in the water under

turbulent conditions favoured by strong winds and meltwater discharges. Lower abundance of Cyclotella and sharp fluctuations in the *Aulacoseira-Staurosira* indicate shorter ice cover periods and increased thermal stratification in the lake. The dominance of Surirella in DZ1b indicates a change to slightly acidic and mesohalobe waters, low nutrients concentration and high light availability in the lake (Morais et al., 2018), suggesting variations in the water level that trend towards a slight decrease. A similar change has been recognised from other environmental records in a close time window, for both sides of the Andean range, and was related to SWW strength. For example, on the windward side of the Andes, Moreno et al. (2009) recorded in Lago Guanaco a high fire activity associated with a decline in precipitation (650–350 BC), while on the lee side, a wet period was recognised by changes in floristic composition and fluctuating water levels in Lake Potrok Aike (Kliem et al., 2013; Wille et al., 2007).

The geochemical ratios and PC1 change slowly (Figure 7). A marked change occurs from 58 cm (~230 AD), that is just after the sedimentation of the medium sand interval (61–65 cm). Those ratios may record either direct tephra deposition or post-deposition tephra remobilisation that may be important in SVZ due to climate humid conditions (e.g. Fontijn et al., 2014). The Si/Al profile is roughly parallel to Br/Ti fluctuations. Both ratios reflect the weathering conditions in the lake watershed and the variable detrital inorganic or organic supplies.

(2) DZ2 (55–80 cm, ~200 BC–320 AD) is represented by low abundance of benthic moderate acidophilic diatoms (i.e. Eunotia, Stauroneis *and* Stenopterobia), being characteristic of oligo- to mesotrophic conditions. DZ2 is dominated by Surirella spp (⩽99% of abundance – Figure 6). Surirella is a common genus semi or loosely attached assigned as benthic but could become planktonic with sufficient turbulence (Bradbury, 1997). For instance, this taxon was recorded as planktonic in tropical lakes (e.g. Brazilian reservoir – Morais et al., 2018) characterised by ⩾10 m depth, slightly acid water (pH 6), high light availability and low nutrient concentrations corresponding to oligotrophic conditions. At Lake Esponja the presence of this taxon associated to the presence of Stenopterobia, a genus also described in the Brazilian reservoirs (Morais et al., 2018), probably recorded similar nutrient-poor conditions. Note the nearly absence or very low content of Aulacoseira evidences more water transparency (i.e. low turbid conditions) in the lower part of DZ2a (70–80 cm, ~200 BC–25 AD) than in previous DZ interval. DZ2a corresponds to an oligosaprophic, oligotrophic, very low alkalinity and calm conditions. The presence of gemmosclere and microsclere sponge spicules (<20%) observed between 70 and 80 cm is associated to seasonal fluctuations in lake level and high concentration of dissolved Si (Matteuzzo et al., 2015). The presence in sample DZ2b 55–65 cm of Aulacoseira records more turbid conditions due to sudden detrital inputs and nutrient availability in the lake. The appearance of Eunotia at the base of DZ2a indicates more acid conditions that will be more steady in DZ3. Volcanic deposits observed along the core caused several changes in redox and pH conditions, increase turbidity and nutrient release that affect the composition in the diatom record including acidification (Kilian et al., 2003).

(3) DZ3 (0–57 cm, 255–2014 AD) shows a remarkable change in environmental conditions in the lake. Staurosira disappears from the record and there is an evident shift in Surirella and *Aulacoseira.* Frustulia spp. and Eunotia spp. become characteristic in the upper record and represent benthic acidophilic to acidobiontic species with optimum pH ranging from 3.6 to 6 (De Nicola, 2000). Frustulia is commonly found in Patagonian lakes and bogs in sites with cold monthly averaged air temperature (4.2°C), acid ($3.6 < pH < 5.5$) and low dissolved organic carbon ($DOC < 20$ mg/l) waters (Casa et al., 2018). The presence of other epiphytic (Epithemia) benthic (Stauroneis, Cymbopleura*)* and a decrease of planktonic (Aulacoseira ambigua) taxa suggest an expansion of the wetland surrounding the lake and less turbid conditions in a more productive watershed. The common presence (⩽30%) of Aulacoseira and Eunotia indicates a closed, more acid environment. This abrupt change in diatom composition with the predominance of Frustulia and Eunotia may be a consequence of the fault rejuvenation at ~2 kyr BP. The occurrence of phytolites in the last 30 cm of LEs14 record underlines an active erosion around the basin.

Conclusions

The Lake Esponja sediments record a temporal evolution over the last ⩽3.5 kyr of allochthonous, detrital and volcanic supplies, combined to variable autochthonous contribution in relation with diatom productivity in the water column.

The glass shard major element composition of identified tephra layers gives a record of past major eruptions related to eruptions of regional volcanoes Mentolat (MEN1700), Macá (i.e. MAC1) and Hudson (HU2200, HU2).

The diatom assemblages evidence variable water column conditions in terms of pH, lake depth and turbidity conditions. The dominance of Aulacoseira and Staurosira emphasises turbid lake conditions over the first part of the lake evolution (DZ1 150–80 cm, ~2 kyr BC–140 BC), likely related to the precipitation associated with the SWW variability. The high abundance of Surirella marks a change to more stable conditions, with no or low runoff in DZ2a. Within the upper zone (DZ3, 57 and 0 cm, 255–2014 AD) Frustulia and Eunotia underline an evolution of lake conditions towards acid peat environment. This main evolution supports a closure of the lake initiated ~2 kyr ago. Such change may be driven by a rejuvenation of the local Rio Manihuales Fault in relation with a major regional earthquake along the LOFZ tectonic structure and recorded by a massive deposit described in literature in Aysen fjord ca. 100 AD.

The observed correlation between Si/Al ratio and austral winter precipitation over the 20 century supports that Si/Al may be used, at least for Lake Esponja setting, as a proxy for physical erosion within the watershed. In particular, the higher Si/Al ratios in the lower LEs14 core section (below 80 cm, before 200 BC) record a period of predominantly precipitations leading to a higher lake level and more turbid conditions. Such changes are in agreement with the dominance of *Aulacoseira-Cyclotella-Fragilaria* assemblages in the lower core section. Diatom assemblages are responding to the influence of both volcanic and tectonic activity deposits modulated by climate variations in this southern part of south hemisphere.

Acknowledgements

The authors thank all the persons who contributed for the sample preparation, analyses and/or figure elaboration, in particular I. Billy (UMR EPOC, Université de Bordeaux, France) for XRF core scanner and Scopix measurements, J. Otten from University of Liege for grain-size analysis and Alex Henríquez from the University of Concepcion for the elaboration of the geological map.

Funding

The author(s) disclosed receipt of the following financial support for the research, authorship, and/or publication of this article: This research was partially funded by bilateral cooperation program Wallonia-Brussels International WBI-Chili, ANID/Fondecyt projects 1201277 and 11201231. D. Álvarez, R. Urrutia and P Pedreros thank to CRHIAM ANID/FONDAP 15130015.

ORCID iDs

Nathalie Fagel https://orcid.org/0000-0002-8231-8295
Sabine Schmidt https://orcid.org/0000-0002-5985-9747

Supplemental material

Supplemental material for this article is available online.

References

Aitchison J (1986) *The Statistical Analysis of Compositional Data*. London: Chapman and Hall.

Appleby PG and Oldfield F (1978) The calculation of lead-210 dates assuming a constant rate of supply of unsupported ^{210}Pb to the sediment. *CATENA* 5: 1–8.

Battarbee RW, Jones VJ, Flower RJ et al. (2001) Diatoms. In: Last W and Smol J (eds) *Tracking Environmental Change Using Lake Sediments, Volume 3: Terrestrial, Algal, and Siliceous Indicators*. Dordrecht: Kluwer Academic Publishers, pp.155–202.

Bertrand S, Araneda A, Vargas P et al. (2012) Using the N/C ratio to correct bulk radiocarbon ages from lake sediments: Insights from Chilean Patagonia. *Quaternary Geochronology* 12: 23–29.

Bertrand S, Hughen K, Sepúlveda J et al. (2014) Late Holocene covariability of the southern westerlies and sea surface temperature in northern Chilean Patagonia. *Quaternary Science Reviews* 105: 195–208.

Bicudo DC, Tremarin PI, Almeida PD et al. (2016) Ecology and distribution of *Aulacoseira* species (Bacillariophyta) in tropical reservoirs from Brazil. *Diatom Research* 31(3): 199–215.

Bizama G, Torrejón F, Aguayo M et al. (2011) Pérdida y fragmentación del bosque nativo en la cuenca del río aysén (Patagonia-Chile) durante el siglo XX. *Revista de Geografía Norte Grande* 49: 125–138.

Blaauw MJ, Christen A and Aquino Lopez MA (2021) Rbacon: Age-Depth Modelling using Bayesian Statistics. R package version 2.5.*3*. Available at: https://CRAN.R-project.org/package=rbacon (accessed 18 November 2022).

Bradbury JP (1997) A diatom-based paleohydrologic record of climate change for the past 800 k.y. From Owens Lake, California. *Geological Society of America Special Papers* 317: 99–112.

Bradley RS (1999) *Paleoclimatology: Reconstruction of Climates from the Quaternary. International Geophysics Series*, 2nd edn. San Diego, CA: Academic Press.

Candès EJ, Li X, Ma Y et al. (2011) Robust principal component analysis? *Journal of Association for Computing Machinery* 57(8): 1–37.

Carrevedo ML, Frugone M, Latorre C et al. (2015) A 700-year record of climate and environmental change from a high Andean lake: Laguna del Maule, central Chile (36°S). *The Holocene* 25: 956–972.

Carter SJ and Colman SM (1994) Biogenic silica in Lake Baikal sediments: Results from 1990–1992 American cores. *Journal of Great Lakes Research* 20(4): 751–760.

Casa V, Mataloni G and Van de Vijver B (2018) Six new Frustulia species (Bacillariophyta) in Tierra del Fuego peatbogs, Patagonia, Argentina. *Fottea*. 18(1): 55–71.

Cembrano J, Hervé F and Lavenu A (1996) The Liquiñe Ofqui fault zone: A long-lived intra-arc fault system in southern Chile. *Tectonophysics* 259: 55–66.

Cembrano J and Lara L (2009) The link between volcanism and tectonics in the southern volcanic zone of the Chilean Andes: A review. *Tectonophysics* 471: 96–113.

Cembrano J, Schermer E, Lavenu A et al. (2000) Contrasting nature of deformation along an intra-arc shear zone, the Liquiñe–Ofqui fault zone, southern Chilean Andes. *Tectonophysics* 319: 129–149.

Chapron E, Ariztegui D, Mulsow S et al. (2006) Impact of the 1960 major subduction earthquake in northern Patagonia (Chile, Argentina). *Quaternary International* 158: 58–71.

Chapron E, Beck C, Pourchet M et al. (1999) 1822 earthquake-triggered homogenite in Lake Le Bourget (NW alps). *Terra Nova* 11: 86–92.

Charrier R, Pinto L and Rodrigues MPM (2007) Tectonostratigraphic Evolution of the Andean Orogen in Chile. In:Moreno T and Gibbsons W (eds) *The Geology of Chile*. London: The Geological Society, pp.21–114.

Croux C, Filzmoser P and Fritz H (2013) Robust sparse principal component analysis. *Technometrics* 55: 202–214.

Cruces F, Urrutia R, Parra O et al. (2006) Changes in diatom assemblages in an andean lake in response to a recent volcanic event. *Archiv fur Hydrobiologie* 165(1): 23–35.

Davies SJ, Lamb HF and Roberts SJ (2015) Micro-XRF core scanning in paleolimnology: Recent developments. In: Croudarce IW and Rothwell RG (eds) *Micro-XRF Studies of Sediment Cores*, vol. 17. Dordrecht: Springer Science, pp.189–226.

Davis JC (2002) *Statistics and Data Analysis in Geology*. New York, NY: John Wiley & sons, p.638.

De Nicola DM (2000) A review of diatoms found in highly acidic environments. *Hydrobiologia* 433: 111–122.

D'Orazio M, Innocenti F, Manetti P et al. (2003) The Quaternary calc-alkaline volcanism of the Patagonian Andes close to the Chile triple junction: Geochemistry and petrogenesis of volcanic rocks from the Cay and maca volcanoes (~45°S, Chile). *Journal of South American Earth Sciences* 16: 219–242.

Elbert J, Wartenburger R, von Gunten L et al. (2013) Late Holocene air temperature variability reconstructed from the sediments of Laguna Escondida, Patagonia, Chile (45°30′S). *Palaeogeography Palaeoclimatology Palaeoecology* 369: 482–492.

Fagel N, Alvarez D, Namur O et al. (2017) Lacustrine record of last millennia eruptions in northern Chilean Patagonia (45–47°S). *The Holocene* 27: 1227–1251.

Fernández M, Björck S, Wohlfarth B et al. (2013) *Diatom assemblage* changes in lacustrine sediments from Isla de los Estados, southernmost South America, in response to shifts in the southwesterly wind belt during the last deglaciation. *Journal of Paleolimnology* 50: 433–446.

Filzmoser P, Fritz H and Kalcher K (2018) PcaPP: Robust PCA by Projection Pursuit. R package version 1.*9-73*. Available at: https://CRAN.R-project.org/package=pcaPP

Finkelstein SA and Gajewski K (2008) Responses of fragilarioid-dominated diatom assemblages in a small Arctic lake to Holocene climatic changes, Russell Island, Nunavut, Canada. *Journal of Paleolimnology* 40: 1079–1095.

Folk RL and Ward WC (1957) Brazos River bar [Texas]: A study in the significance of grain size parameters. *Journal of Sedimentary Petrology* 27: 3–26.

Fontaine CM, Siani G, Delpech G et al. (2021) Post-glacial tephrochronology record off the Chilean continental margin (~41°S). *Quaternary Science Reviews* 261: 106928.

Fontijn K, Lachowycz SM, Rawson H et al. (2014) Late Quaternary tephrostratigraphy of southern Chile and Argentina. *Quaternary Science Reviews* 89: 70–84.

Frugone-Alvarez M, Latorre C, Barreiro-Lostres F et al. (2020) Volcanism and climate change as drivers in holocene depositional dynamic of Laguna del Maule (Andes of central Chile – 36° S). *Climate of the Past* 16: 1097–1125.

Frugone-Alvarez M, Latorre C, Giralt S et al. (2017) A 7000-year high-resolution lake sediment record from coastal central Chile (Lago Vichuquén, 34°S): Implications for past sea level and environmental variability. *Journal of Quaternary Science* 32: 830–844.

Garreaud R, Lopez P, Minvielle M et al. (2013) Large-scale control on the Patagonian climate. *Journal of Climate* 26: 215–230.

Garrett RG (2018) Rgr: Applied Geochemistry EDA. R package version 1.1.*15*. Available at: https://CRAN.R-project.org/package=rgr

Gilli A, Ariztegui D, Anselmetti FS et al. (2005) Mid-Holocene strengthening of the Southern Westerlies in South America - Sedimentological evidences from Lago Cardiel, Argentina (49°S). *Global planetary Change* 49: 75–93.

Grimm EC (1991) *TILIA and TILIA GRAPH*. Springfield, IL: Illinois State Museum.

Grimm EC, Maher LJ and Nelson DM (2009) The magnitude of error in conventional bulk-sediment radiocarbon dates from central North America. *Quaternary Research* 72(2): 301–308.

Gutiérrez F, Gioncada A, González Ferran O et al. (2005) The Hudson volcano and surrounding monogenetic centres (Chilean Patagonia): An example of volcanism associated with ridge–trench collision environment. *Journal of Volcanology and Geothermal Research* 145: 207–233.

Guyard H, Chapron E, St-Onge G et al. (2007) High-altitude varve records of abrupt environmental changes and mining activity over the last 4000 years in the western French alps (Lake Bramant, Grandes Rousses Massif). *Quaternary Science Reviews* 26: 2644–2660.

Haberle SG and Lumley SH (1998) Age and origin of tephras recorded in postglacial lake sediments to the west of the southern Andes, 44°S to 47°S. *Journal of Volcanology and Geothermal Research* 84: 239–256.

Harris IC and Jones PD (2020) CRU TS4.03: Climatic Research Unit (CRU) Time-Series (TS) version 4.03 of high-resolution gridded data of month-by-month variation in climate. *Centre for Environmental Data Analysis*. DOI: 10.5285/10d3e3640f004c578403419aac167d82

Hartley B, Barber HG, Carter JR et al. (1996) *An Atlas of British Diatoms*. Bristol: Biopress Ltd.

Hedges JI and Stern JH (1984) Carbon and nitrogen determinations of carbonate-containing solids1. *Limnology and Oceanography* 29(3): 657–663.

Heiri O, Lotter AF and Lemcke G (2001) Loss on ignition as a method for estimating organic and carbonate content in sediments: Reproducibility and comparability of results. *Journal of Paleolimnology* 25(1): 101–110.

Hepp C, Reyes C and Muñoz R (2018) *Análisis de Datos Históricos de Cinco Estaciones Meteorológicas de La Región de Aysén. Boletín Técnico N°365*. Coyhaique, Aysén-Patagonia: Instituto de Investigaciones Agropecuarias, Centro de Investigación INIA Tamel Aike (in Spanish).

Hervé F (1994) The Southern Andes between 39j and 44jS latitude: The geological signature of a transpressive tectonic regime related to a magmatic arc. In: Reutter K-J, Scheuber E and Wigger PJ (eds) *Tectonics of the Southern Central Andes*. Berlin: Springer, pp.243–248.

Hickey RL, Frey FA, Gerlach DC et al. (1986) Multiple sources for basaltic arc rocks from the Southern Volcanic Zone of the Andes (34°–41°S): Trace element and isotopic evidence for contributions from subducted oceanic crust, mantle, and continental crust. *Journal of Geophysical Research* 91: 5963–5983.

Hickey-Vargas R, Sun M, López-Escobar L et al. (2002) Multiple subduction components in the mantle wedge: Evidence from eruptive centers in the central Southern volcanic zone, Chile. *Geology* 30(3): 199–202.

Hickey-Vargas RL, Moreno-Roa H, López-Escobar L et al. (1989) Geochemical variations in Andean basaltic and silicic lavas from the Villarrica-Lanín volcanic chain (39.5°S): An evaluation of source heterogeneity, fractional crystallization and crustal assimilation. *Contributions to Mineralogy and Petrology* 103: 361–386.

Hill MO and Gauch HG (1980) Detrended correspondence analysis: An improved ordination technique. *Vegetatio* 42: 47–58.

Hogg AG, Hua Q, Blackwell PG et al. (2013) SHCal13 Southern Hemisphere calibration, 0–50,000 years cal BP. *Radiocarbon* 55(4): 1889–1903.

Juggins S (2017) Rioja: Analysis of Quaternary Science Data, R package version (0.*9-21)*. Available at: http://cran.r-project.org/package=rioja

Kalugin I, Darin A, Rogozin D et al. (2013) Seasonal and centennial cycles of carbonate mineralisation during the past 2500 years from varved sediment in Lake Shira, South Siberia. *Quaternary International* 290–291: 245–252.

Kanamori H (1977) The energy release in great earthquakes. *Journal of Geophysical Research* 82: 2981–2987.

Kilian R, Hohner M, Biester H et al. (2003) Holocene peat and lake sediment tephra record from the southernmost Chilean Andes (53-55°S). *Revista geologica de Chile* 30: 47–64.

Kliem P, Buylaert JP, Hahn A et al. (2013) Magnitude, geomorphologic response and climate links of lake level oscillations at Laguna Potrok Aike, Patagonian steppe (Argentina). *Quaternary Science Reviews* 71: 131–146.

Krammer K and Lange-Bertalot H (1986) *Süßwasserflora von Mitteleuropa, Bacillariophyceae Volume 2/1: Naviculaceae*. Jena: Gustav Fischer Verlag.

Krammer K and Lange-Bertalot H (1988) *Süßwasserflora von Mitteleuropa, Bacillariophyceae, Volume 2/2: Bacillariacae, Epithemiaceae, Surirellaceae*. New York, NY: Gustav Fischer Verlag.

Krammer K and Lange-Bertalot H (1991a) *Süßwasserflora von Mitteleuropa, Bacillariophyceae, Volume 2/3: Centrales, Fragilariaceae, Eunotiaceae*. Berlin: Spektrum Akademischer Verlag Heidelberg.

Krammer K and Lange-Bertalot H (1991b) *Süßwasserflora von Mitteleuropa, Bacillariophyceae, Volume 2/4: Achnanthaceae, Kritische Ergänzungen Zu Navicula (Lineolatae) und Gomphonema*. New York, NY: Gustav Fischer Verlag.

Kratzmann DJ, Carey S, Scasso RA et al. (2010) Role of cryptic amphibole crystallization in magma differentiation at Hudson volcano, Southern Volcanic Zone, Chile. *Contributions to Mineralogy and Petrology* 159: 237–264.

Kylander ME, Ampel L, Wohlfarth B et al. (2011) High-resolution X-ray fluorescence core scanning analysis of Les echets (France) sedimentary sequence: New insights from chemical proxies. *Journal of Quaternary Science* 26: 109–117.

Kylander ME, Lind EM, Wastegård S et al. (2012) Recommendations for using XRF core scanning as a tool in tephrochronology. *The Holocene* 22: 371–375.

Lange-Bertalot H, Rumrich U and Rumrich M (2000) Diatoms of the Andes (From Venezuela to Patagonia/ Tierra Del Fuego). *Iconografia diatomologica* 9: 1–673.

Legrand D, Barrientos S, Bataille K et al. (2011) The fluid-driven tectonic swarm of Aysen Fjord, Chile (2007) associated with two earthquakes (Mw=6.1 and mw=6.2) within the Liquiñe-Ofqui Fault Zone. *Continental Shelf Research* 31: 154–161.

Leinen M (1977) A normative calculation technique for determining opal in deep-sea sediments. *Geochimica et Cosmochimica Acta* 41(5): 671–676.

López-Escobar L, Cembrano J and Moreno H (1995a) Geochemistry and tectonics of the chilean southern Andes basaltic Quaternary volcanism (37º-46ºS). *Revista Geológica de Chile* 22(2): 219–234.

López-Escobar L, Parada MA, Hickey-Vargas R et al. (1995b) Calbuco volcano and minor eruptive centers distributed along the Liquiñe-ofqui Fault Zone, Chile (41°-42°S): Contrasting origin of andesitic and basaltic magma in the Southern Volcanic Zone of the Andes. *Contributions to Mineralogy and Petrology* 119: 345–361.

López-Escobar L, Kilian R, Kempton P et al. (1993) Petrology and geochemistry of Quaternary rocks from the southern volcanic zone of the Andes between 41°30′ and 46°00′S, Chile. *Revista Geológica de Chile* 20(1): 33–55.

Lowe DJ (2011) Tephrochronology and its application: A review. *Quaternary Geochronology* 6: 107–153.

Luebert F and Pliscoff P (2006) *Sinopsis Bioclimática y Vegetacional de Chile*. Santiago: Editorial Universitaria.

Markgraf V (1993) Paleoenvironments and paleoclimates in Tierra del Fuego and southernmost Patagonia, South America. *Palaeogeography Palaeoclimatology Palaeoecology* 102(1-2): 53–68.

Markgraf V, Bradbury JP, Schwalb A et al. (2003) Holocene palaeoclimates of southern Patagonia: Limnological and environmental history of Lago Cardiel, Argentina. *The Holocene* 13(4): 581–591.

Matteuzzo MC, Volkmer-ribeiro C, Varajão AFD et al. (2015) Environmental factors related to the production of a complex set of spicules in a tropical freshwater sponge. *Anais da Academia Brasileira de Ciencias* 87(4): 2013–2029.

Mella M, Ramos A, Kraus S et al. (2012) *Datos Tefroestratigraphicos de Erupciones Holocenas del Volcan Mentolat, Andes del Sur (44°40'S), Chile*. Antofagasta: Congreso Geológico Chileno.

Moernaut J, Daele MV, Heirman K et al. (2014) Lacustrine turbidites as a tool for quantitative earthquake reconstruction: New evidence for a variable rupture mode in south central Chile. *Journal of Geophysical Research-Solid Earth* 119: 1607–1633.

Moernaut J, De Batist M, Charlet F et al. (2007) Giant earthquakes in south-central Chile revealed by holocene mass-wasting events in Lake Puyehue. *Sedimentary Geology* 195(3–4): 239–256.

Moore D and Reynolds RC Jr (1997) *X-Ray Diffraction and the Identification and Analysis of Clay Minerals*. Oxford: Oxford University Press.

Morais KSD, Bartozek ER, Zorzal-Almeida S et al. (2018) Taxonomy and ecology of order Surirellales (Bacillariophyceae) in tropical reservoirs in Southeastern of Brazil. *Acta Limnologica Brasiliensia* 30: 204.

Morales EA, Wetzel CE, Rivera SF et al. (2014) Current taxonomic studies on the diatom flora (Bacillariophyceae) of the Bolivian Altiplano, South America, with possible consequences for palaeoecological assessments. *Journal of Micropalaentology* 33: 121–129.

Moreiras SM (2005) Climatic effect of ENSO associated with landslide occurrence in the Central Andes, Mendoza Province, Argentina. *Landslides* 2: 53–59.

Moreno PI, François JP, Villa-Martínez RP et al. (2009) Millennial-scale variability in southern hemisphere westerly wind activity over the last 5000 years in SW Patagonia. *Quaternary Science Reviews* 28: 25–38.

Mueller UA and Grunsky EC (2016) Multivariate spatial analysis of lake sediment geochemical data, Melville Peninsula, Nunavut, Canada. *Applied Geochemistry* 75: 247–262.

Naranjo JA and Stern CR (1998) Holocene explosive activity of Hudson Volcano, southern Andes. *Bulletin of Volcanology* 59: 291–306.

Naranjo JA and Stern CR (2004) Holocene tephrochronology of the southernmost part (42°30'-45°S) of the Andean Southern Volcanic Zone. *Revista Geologica de Chile* 31(2): 225–240.

Ohlendorf C and Sturm M (2008) A modified method for biogenic silica determination. *Journal of Paleolimnology* 39(1): 137–142.

Oksanen J, Blanchet FG, Friendly M et al. (2019) Vegan: Community Ecology Package. R package version 2.*5-6*. Available at: https://CRAN.R-project.org/package=vegan

Óladóttir BA, Sigmarsson O, Larsen G et al. (2011) Provenance of basaltic tephra from Vatnajökull subglacial volcanoes, Iceland, as determined by major- and trace-element analyses. *The Holocene* 21: 1037–1048.

Pankhurst RJ, Weaver SD, Hervé F et al. (1999) Mesozoic-Cenozoic evolution of the North Patagonian batholith in Aysen, southern Chile. *Journal of the Geological Society* 156: 673–694.

Peel MC, Finlayson BL and McMahon TA (2007) Updated world map of the Köppen-Geiger climate classification. *Hydrology and Earth System Sciences Discussions, European Geosciences Union* 11(5): 1633–1644.

Perren BB, Hodgson DA, Roberts SJ et al. (2020) Southward migration of the southern hemisphere westerly winds corresponds with warming climate over centennial timescales. *Communications Earth & Environment* 1: 58.

R Development Core Team (2018) *R: A Language and Environment for Statistical Computing*. Vienna: R Foundation for Statistical Computing. Available at: http://www.R-project.org/

Revelle W (2017) *Psych: Procedures for Personality and Psychological Research*. Evanston, IL: North-Western University. Available at: http://personality-project.org/r/psych

Sellés D, Rodríguez AC, Dungan MA et al. (2004) Geochemistry of Nevado de Longaví volcano (36.2°S): A compositionally atypical arc volcano in the Southern Volcanic Zone of the Andes. *Revista Geológica de Chile* 31(2): 293–315.

Sepúlveda SA, Rebolledo S and Vargas G (2006) Recent catastrophic debris flows in Chile: Geological hazard, climatic relationships and human response. *Quaternary International* 158: 83–95.

SERNAGEOMIN (2003) Mapa Geológico de Chile 1:1000000: versión digital. Gobierno de Chile, Servicio Nacional de Geología y Minería, Publicación Geológica Digital, No. 4 (CD-ROM, versión1.0, 2003). Santiago, Chile.

SERNAGEOMIN (2012) Investigatión geológica minera ambiantal en Aysén (Codigo BIP No. 30036527-0). Resumen ejecutivo y synthesis de localidades. Report, Servicio Nacional de Geología y Minería Santiago, Chile.

Siebert L, Simkin T and Kimberly P (2010) *Volcanoes of the World*, 3rd edn. Berkeley, CA: University of California Press.

Siegenthaler C and Sturm M (1991) Slump induced surges and sediment transport in Lake Uri, Switzerland. *SIL Proceedings* 24(2): 955–958.

Stern CR (2004) Active Andean volcanism: its geologic and tectonic setting. *Revista Geologica del Chile* 31(2): 161–206.

Stern CR, de Porras ME and Maldonado A (2015) Tephrochronology of the upper Rio Cisnes valley (44°S), southern Chile. *Andean Geology* 42: 173–189.

Stupar YV, Schäfer J, García MG et al. (2014) Historical mercury trends recorded in sediments from the Laguna del Plata, Córdoba, Argentina. *Chemie der Erde Geochimistry* 74: 353–363.

Thomson SN (2002) Late Cenozoic geomorphic and tectonic evolution of the Patagonian Andes between latitudes 42°S and 46°S: An appraisal based on fission-track results from the transpressional intra-arc Liquiñe-Ofqui fault zone. *Geological Society of America Bulletin* 114(9): 1159–1173.

Van Daele M, Moernaut J, Doom L et al. (2015) A comparison of the sedimentary records of the 1960 and 2010 great Chilean earthquakes in 17 lakes: Implications for quantitative lacustrine palaeoseismology. *Sedimentology* 62: 1466–1496.

Van Daele M, Versteeg W, Pino M et al. (2013) Widespread deformation of basin-plain sediments in Aysén fjord (Chile) due

to impact by earthquake-triggered, onshore-generated mass movements. *Marine Geology* 337: 67–79.

Van de Vijver B, Frenot Y and Beyens B (2002) Freshwater Diatoms from Ile de la Possission (Crozet Archipelago, Subantartica). *Bibliotheca Diatomologica* 46: 1–412.

Vanneste K, Wils K and Van Daele M (2018) Probabilistic evaluation of fault sources based on paleoseismic evidence from mass-transport deposits: The example of Aysén Fjord, Chile. *Journal of Geophysical Research Solid Earth* 123: 9842–9865.

Villa-Martinez R, Moreno PI and Valenzuela MA (2012) Deglacial and postglacial vegetation changes on the eastern slopes of the central Patagonian Andes (47°S). *Quaternary Science Reviews* 32: 86–99.

Waldmann N, Anselmetti FS, Ariztegui D et al. (2011) Holocene mass-wasting events in Lago Fagnano, Tierra del Fuego (54°S): Implications for paleoseismicity of the magallanes-Fagnano transform fault. *Basin Research* 23: 171–190.

Wang M, Zheng H, Xie X et al. (2011) A 600-year flood history in the Yangtze River drainage: Comparison between a subaqueous delta and historical records. *Chinese Science Bulletin* 56: 188–195.

Watt SFL, Pyle DM and Mather TA (2013) The volcanic response to deglaciation: Evidence from glaciated arcs and a reassessment of global eruption records. *Earth Science Review* 122: 77–102.

Weller D, Miranda CG, Moreno PI et al. (2014) The large lateglacial Ho eruption of the Hudson volcano, southern Chile. *Bulletin of Volcanology* 76: 831.

Weller D, Miranda CG, Moreno PI et al. (2015) Tephrochronology of the Southernmost Andean soutertn Volcanic zone, Chile. *Bulletin of Volcanology* 77: 107.

Wille M, Maidana NI, Schäbitz F et al. (2007) Vegetation and climate dynamics in southern South America: The microfossil record of Laguna Potrok Aike, Santa Cruz, Argentina. *Review of Palaeobotany and Palynology* 146: 234–246.

Wils K, Van Daele M, Kissel C et al. (2020) Seismo-Turbidites in Aysén Fjord (southern Chile) reveal a complex pattern of rupture modes along the 1960 megathrust earthquake segment. *Journal of Geophysical Research Solid Earth* 125: e2020JB019405.

Wils K, Van Daele M, Lastras G et al. (2018) Holocene event record of Aysén Fjord (Chilean Patagonia): An interplay of volcanic eruptions and crustal and megathrust earthquakes. *Journal of Geophysical Research Solid Earth* 123: 324–343.

Witak M, Hernández-Almeida I, Grosjean M et al. (2017) Diatom-based reconstruction of trophic status changes recorded in varved sediments of Lake żabińskie (northeastern Poland), AD 1888-2010. *Oceanological and Hydrobiological Studies* 46(1): 1–17.

Żarczyński M, Wacnik A and Tylmann W (2019) Tracing lake mixing and oxygenation regime using the Fe/Mn ratio in varved sediments: 2000 year-long record of human-induced changes from Lake żabińskie (NE Poland). *The Science of the Total Environment* 657: 585–596.

Ziegler M, Jilbert T, de Lange GJ et al. (2008) Bromine counts from XRF scanning as an estimate of the marine organic carbon content of sediment cores. *Geochemistry Geophysics Geosystems* 9: Q05009.